

Development of a Nanohybrid Peptide Hydrogel for Enhanced Intervertebral Disc Repair and Regeneration

Brian M. Conley,[§] Letao Yang,[§] Basanta Bhujel, Jeffrey Luo, Inbo Han,^{*} and Ki-Bum Lee^{*}



Cite This: <https://doi.org/10.1021/acsnano.2c11441>



Read Online

ACCESS |



Metrics & More



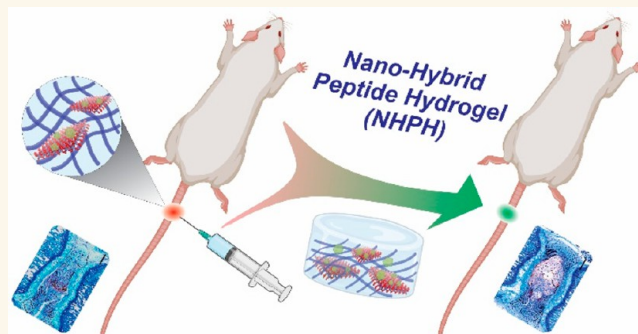
Article Recommendations



Supporting Information

ABSTRACT: Effective therapeutic approaches to overcome the heterogeneous pro-inflammatory and inhibitory extracellular matrix (ECM) microenvironment are urgently needed to achieve robust structural and functional repair of severely wounded fibrocartilaginous tissues. Herein we developed a dynamic and multifunctional nanohybrid peptide hydrogel (NHPH) through hierarchical self-assembly of peptide amphiphile modified with biodegradable two-dimensional nanomaterials with enzyme-like functions. NHPH is not only injectable, biocompatible, and biodegradable but also therapeutic by catalyzing the scavenging of pro-inflammatory reactive oxygen species and promoting ECM remodeling. In addition, our NHPH method facilitated the structural and functional recovery of the intervertebral disc (IVD) after severe injuries by delivering pro-regenerative cytokines in a sustained manner, effectively suppressing immune responses and eventually restoring the regenerative microenvironment of the ECM. In parallel, the NHPH-enhanced nucleus pulposus cell differentiation and pain reduction in a rat nucleotomy model further validated the therapeutic potential of NHPH. Collectively, our advanced nanoscaffold technology will provide an alternative approach for the effective treatment of IVD degeneration as well as other fibrocartilaginous tissue injuries.

KEYWORDS: nanohybrid peptide hydrogel, nanoscaffolds, advanced tissue engineering, growth and differentiation factor, intervertebral disc repair, disc degeneration



Fibrocartilaginous tissue injuries, such as intervertebral disc (IVD) degeneration and knee meniscus tears, are often associated with debilitating pain and loss of mobility, thereby significantly compromising patients' quality of life.^{1,2} Despite the enormous socioeconomic burden caused by diseases and injuries to fibrocartilaginous tissues, the development of effective treatments for the functional restoration of degenerative fibrocartilage tissues is still limited.^{1,3} This is mainly due to several critical issues in degenerative/injury tissue microenvironments, including restricted regeneration ability, pro-inflammatory factors, and the heterogeneous extracellular matrix (ECM).^{2,4–7} State-of-the-art tissue engineering approaches, such as stem cell-based therapies, demonstrated some potential to dynamically modulate the regeneration of fibrocartilaginous tissues.^{8–13} Nevertheless, their efficacy is currently limited by the lack of modulation of stem cell differentiation into target soft tissues required for functional restoration.^{14–16}

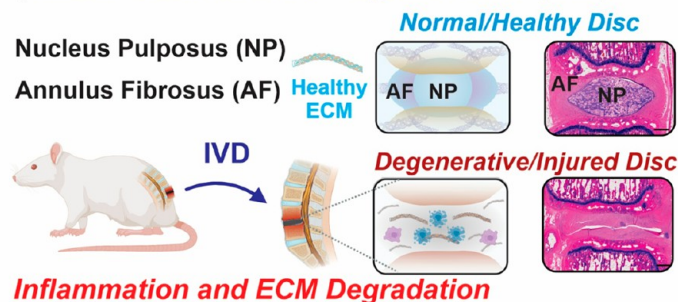
Biomaterial-based approaches (e.g., nanoscaffolds and drug-loaded nanomaterials) have greatly facilitated the engineering of

fibrocartilaginous tissues by addressing the aforementioned challenges. These approaches can improve the release of biologics, provide mechanical support, and replace unfavorable ECM after injury.^{4,15,17–31} However, crosstalk between different inhibitory signaling pathways has compound effects on the outcome of nanomaterial-based tissue engineering.^{32–35} One such complicated inhibitory signal is degeneration-associated reactive oxygen species (ROS) that cause continuous apoptosis, inflammation, and uncontrollable differentiation of endogenous stem cells during acute injury and chronic phases of degeneration. Another barrier arises from the multiscale and heterogeneous ECM structures and mechanical environments

Received: November 16, 2022

Accepted: February 9, 2023

a) Intervertebral Disc Degeneration (IVD)

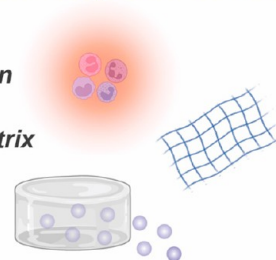


b) Key Challenges in Therapies For IVD

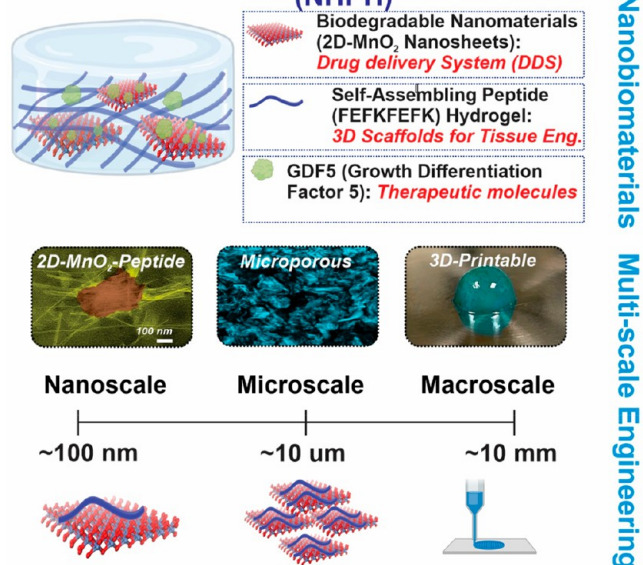
Promoting Cell Proliferation

Restoring Extracellular Matrix

Developing Non-invasive Monitoring methods



c) Biodegradable/Injectable Nano-Hybrid Peptide Hydrogel (NHPH)



d) Enhanced Intervertebral Disc Repair Using NHPH

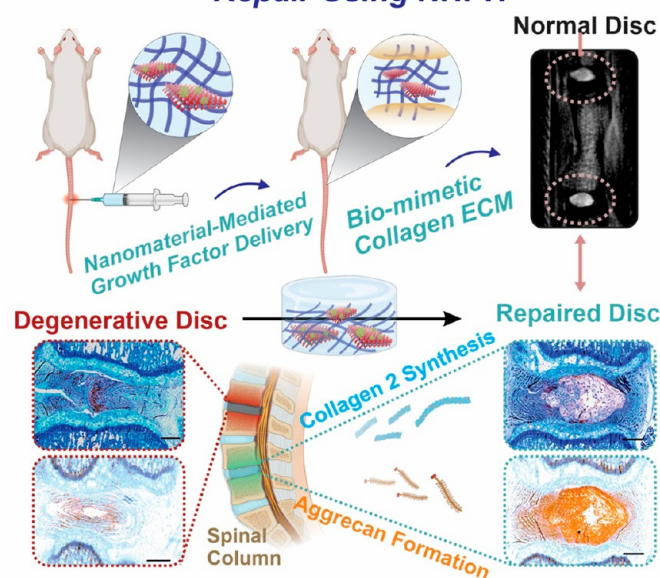


Figure 1. NHPH provides a biodegradable therapeutic platform to regenerate ECM during disc degeneration that further leads to robust tissue regeneration and functional outcomes. (a) IVD is caused by the loss of annulus fibrosus and nucleus pulposus cells driven by an inflammatory reaction which secretes ECM-degrading enzymes. (b) Conventional biomaterials (i.e., biopolymers) may not directly address inflammation and the damaged ECM environment leading to chronic pain. (c) Two-dimensional manganese dioxide (2D-MnO₂) nanomaterial NHPH has hierarchical structures to recapitulate natural fibril-like ECM on the nanoscale (i.e., fibril-like β -sheets), microscale (supramolecular assemblies), and macroscale (3D-printed hydrogels). (d) NHPH loaded with GDF-5 injected into the IVD restores IVD tissue similar to that of uninjured discs while stimulating both collagen and aggrecan secretion and spatially regenerating annulus fibrosus and nucleus pulposus regions.

typically associated with fibrocartilaginous tissues.^{36,37} For example, an IVD injury, such as a degenerative condition associated with disc injuries, is characterized by an inner circular region (nucleus pulposus, abbreviated as NP) with gel-like properties and a peripheral annulus fibrosus (AF) region with ligament-like properties (Figure 1a).³ Hence, designing and developing biomaterials to dynamically modulate and restore homeostasis and functions of disc tissues is thus extremely challenging.³¹ Last, pain management in fibrocartilage degeneration represents another challenge, as even functional restoration of tissue does not ensure pain relief because of relatively poorly understood pain signaling.^{16,38} Therefore, there is an urgent need to develop advanced tissue engineering methods for effectively treating fibrocartilage degeneration. A dynamic and multifunctional bionanomaterial system with tunable biophysical and biochemical properties can significantly improve existing therapies for fibrocartilaginous tissue damage.

Herein, we developed a multifunctional and dynamic nanohybrid peptide hydrogel (NHPH)-based approach that can restore a healthy ECM microenvironment in the damaged IVD region, alleviate ROS-induced inflammation, and enhance cartilaginous cell differentiation, thereby promoting fibrocartilaginous tissue regeneration (Figure 1). Recently, dynamic hydrogels based on self-assembled peptide amphiphiles (PAs) with simultaneous drug release and adaptable ECM environments were developed for treating soft tissue damages like spinal cord injury.^{39,40} We modified the PA system and incorporated biodegradable nanomaterials into the self-assembling PA system (Figure 1c) that can: (i) strongly bind to peptides and modulate mechanical properties of PAs, (ii) scavenge ROS to reduce inflammation, and (iii) promote drug-hydrogel interactions to guide cartilaginous differentiation. As a proof-of-concept, the NHPH was tailored and successfully applied for IVD regeneration. Specifically, the NHPH was assembled from 1D dynamic peptide nanofibrils and growth differentiation factor 5

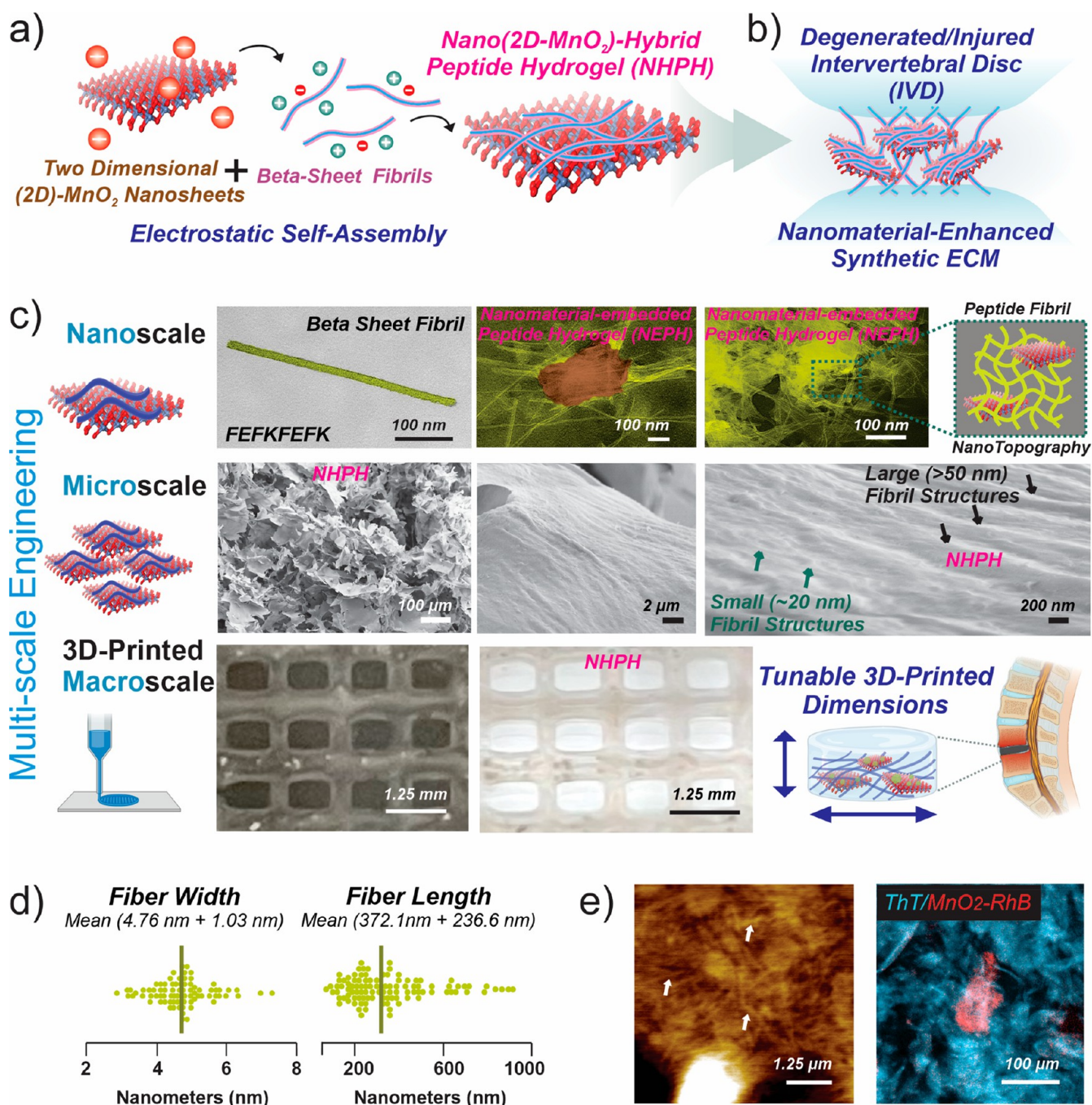


Figure 2. 2D- MnO_2 nanosheets integrated with self-assembling peptides form hybrid inorganic/organic nanostructures which mimicks natural ECM promote a favorable ECM microenvironment through hierarchal cues. (a) Negatively charged 2D- MnO_2 nanosheets interact with β -sheet-forming synthetic peptides (FEFKFEFK) through electrostatic interactions to form hybrid nanosheet-fibril structures. (b) Hybrid inorganic/organic NHPH retains injectable hydrogel properties observed in conventional self-assembling peptide hydrogels. (c) The first row describes that the nanoscale features, imaged with TEM, demonstrate individual β -sheet peptide fibers (left panel), hybrid nanosheet-fibril structures (middle panel), and larger hybrid composites (right panel). Images are pseudocolored (red color, MnO_2 ; yellow color, peptide fibers). The second row describes that the microscale features, imaged with SEM, of lyophilized NHPH demonstrate a porous structure, favorable for cellular extension and penetration. The third row describes that the 3D-printed NHPH with different sizes and shapes exhibiting versatility to fabricate a wide range of dimensions to treat various injuries and conditions. (d) Quantification of peptide fibrils from TEM images. (e) AFM (image on the left) and confocal imaging (on the right) stained with thioflavin T (ThT) and with rhodamine b (RhB)-loaded 2D- MnO_2 nanosheets.

(GDF-5)-loaded 2D ROS-scavenging MnO_2 nanosheets that function as nanozymes for treating disc tissue degeneration. The NHPH is shear thinning, demonstrates a similar stiffness to healthy disc tissues, modulates drug release through its tunable porosity, and can be 3D-printed into shapes matching the injury

sites; injection of our tailored NHPH into injured IVDs resulted in considerable regeneration of NP tissue, including restoration of critical ECM components (e.g., aggrecan and collagen), reduction of pain biomarkers, and enhanced cartilage regeneration. Therefore, our developed NHPH system may facilitate

a) Nanomaterial-Enabled Modulation of Biophysical Cues Combined Therapeutic Effects

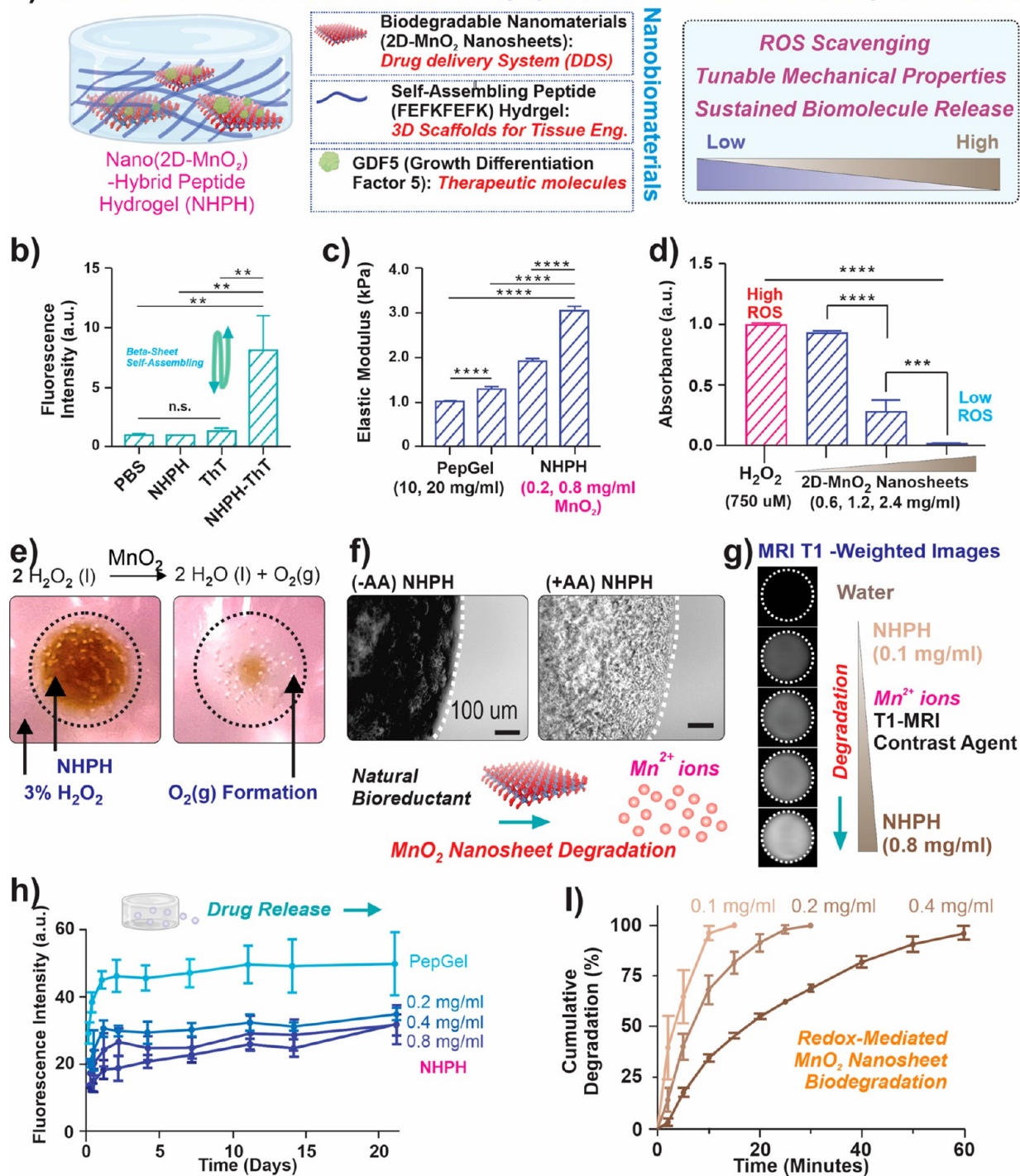


Figure 3. Biodegradable 2D-MnO₂ nanosheets demonstrate tunable biophysical and biochemical properties to potentially enhance overall therapeutic effects. (a) NHPH can provide a versatile platform to load growth factors and self-assembling peptides. (b) Fluorescence intensity of thioflavin T (ThT) shows octapeptide PepGel hydrogels self-assemble to form secondary β -sheet structures. (c) Rheological data, derived from oscillatory shear strain, showing hydrogel elastic modulus can be tuned by varying the concentration of 2D-MnO₂ nanosheets (0.2 mg/mL, low and 0.8 mg/mL high) to render hydrogel stiffness (\sim 1–3 kPa) comparable to natural host tissue such as the nucleus pulposus in the IVD (\sim 6 kPa). (d) Peroxide detection assay where greater absorbance indicates a higher concentration of H₂O₂. An increasing concentration of 2D-MnO₂ nanosheets scavenges a greater degree of peroxides. (e) Macroscopic images exhibiting the formation of oxygen gas bubbles during accelerated H₂O₂ decomposition. (f) Phase images of the degradation of 2D-MnO₂ nanosheets in NHPH after the treatment of ascorbic acid. (g) MRI T1 signal from ascorbic acid-treated NHPH which release T1 contrast agent Mn²⁺ upon degradation. (h) Fluorescence intensity of model growth factor FITC-insulin release from NHPH with tunable concentrations of nanosheets demonstrating a more sustained release with increasing concentration. $^{**}p < 0.005$, $^{***}p = 0.0002$, and $^{****}p < 0.0001$ by ordinary one-way ANOVA with Tukey's multiple-comparisons test. n.s. means no significance.

the engineering of fibrocartilage tissues after injuries or diseases (Figure 1d).

RESULTS AND DISCUSSION

The ECM environment predominantly comprises proteins, such as collagen, which self-assemble into one-dimensional fibril-like structures.^{41,42} Dynamic PA hydrogels can provide an adaptable ECM environment that has recently shown excellent potential for tissue regeneration postspinal cord injury.^{39,43} Inspired by this, we further incorporated biodegradable 2D-MnO₂ nanosheets into octapeptide-based PA self-assembled systems to develop the NHPH, which hierarchically mimics natural ECM while simultaneously providing ROS-scavenging capabilities (Figure 2). Specifically, nanosheets first absorb and assemble PA units through metal- π and electrostatic interactions, then the alternating hydrophobic [phenylalanine (F)] and hydrophilic [lysine (K) and glutamate (E)] residues in the octapeptides further drive the noncovalent self-assembly through structural packing (Figure 2a,b). The reaction typically completes in a few minutes, allowing sufficient time for the injection into injured disc tissues, and also occurs in water or phosphate-buffered saline (PBS) with excellent biocompatibility. Transmission electron microscopy (TEM) indicates individual peptide fibers ranging in lengths (~1–10 μ m) and widths (~5–20 nm) (Figure 2c and Figure S1). At a peptide concentration of 5 mg/mL, the average fibril width was approximately 4.7 nm (\pm 1.0 nm), while fibril length was approximately 372 nm (\pm 237 nm) (Figure 2d). It is worth noting that these dimensions closely align with natural collagen fibrils, which may be broken down into monomeric species and then assembled into tropocollagen, fibrils, and supramolecular assemblies.⁴⁴ Introducing synthesized 2D-MnO₂ nanosheets through drop-casting and vigorous vortexing in FEFKFEFK peptide aqueous solutions to form nano (MnO₂)-hybrid peptide hydrogels (NHPH) results in the formation of dense networks of nanosheets and peptide fibrils (Figure 2c and Figure S1). Fibril density increases in regions of 2D-MnO₂ nanosheets, attributable to prevailing electrostatic interactions between polar oxygen functional groups on 2D-MnO₂ nanosheets and hydrophilic lysine and glutamate residues. This increase in fibril density may facilitate cellular adhesion inside *in vivo* microenvironments, which has been demonstrated for both 2D-MnO₂ nanosheets and peptide fibrils.

In addition, cellular penetration and migration within *in vivo* microenvironments may be promoted as scanning electron microscopy (SEM) images of lyophilized NHPH show porous hybrid structures of stacked 2D-MnO₂ nanosheets and peptide fibrils (Figure 2c and Figure S1). Atomic force microscopy (AFM) and confocal microscopy both confirm nanotopographical features and porous structures, respectively (Figure 2e). Moreover, control over the macroscale assembly of biomaterials would also be desirable to precisely design biomaterials to treat intervertebral disc degeneration (IVDD) and other central nervous system injuries and disorders. For this purpose, NHPH was successfully 3D-printed into numerous patterns of varying sizes and dimensions as a proof-of-concept, with the potential to be printed in disc-mimicking structures for future research (Figure 2c).

To create a favorable microenvironment for disc regeneration and monitor the progress of treatment, injectable and self-therapeutic hydrogels that self-assemble from 2D nanosheets with tunable structures, enzyme-like functions, and magnetic resonance imaging (MRI)-active components would be desired for IVD treatment.⁴⁵ We thus optimized the biophysical

properties, biodegradability, mechanical properties, and drug release rates of NHPH by modulating the self-assembly of 2D-MnO₂ nanosheets with PAs (Figure 3). The self-assembly was realized by initially absorbing PAs onto nanosheets under diluted conditions, followed by salt addition that triggered the cross-linking among PA-absorbed nanosheets. We first confirmed the successful formation of NHPH by observing a noticeable difference in morphologies in electron microscopy, with the presence of both 1D nanofibrils and 2D nanosheets, whereas pure PA hydrogels only revealed 1D nanostructures (Figure 3b). Next, we investigated the effect of 2D-MnO₂ nanosheets on NHPH stiffness. The nucleus pulposus region of the IVD is gelatinous, with high-water content, and abundant in type II collagen. Reports suggest the elastic modulus of the nucleus pulposus region is approximately 6 kPa. Here, we observed that NHPH are tunable within a 1–3 kPa range by tuning the concentrations of nanosheets (Figure 3c). Although the nucleolus pulposus region typically has a wider range of stiffness (1–6 kPa), our finding still aligns with previous reports where integrating nanomaterials in peptide hydrogels increases stiffness.⁴⁶ Furthermore, it has been well established that ROS, such as hydrogen peroxide (H₂O₂), are highly secreted during inflammation. These ROS can aggravate intervertebral degeneration by oxidizing proteins and cellular membranes, resulting in disc cell death.⁴⁷ As a result of vascular failure, IVDD can also create a hypoxic microenvironment, restricting nutritional and metabolic diffusion.⁴⁸ However, few biomaterials, and even fewer hybrid nanomaterials, have been designed to address these issues. In this regard, NHPH with 2D-MnO₂ nanosheets can simultaneously provide ROS scavenging while producing oxygen as a byproduct, thereby offering a self-therapeutic outcome. To verify the ROS scavenging effects from nanosheets and NHPH, various concentrations of 2D-MnO₂ nanosheets were incubated in a solution of H₂O₂ (0.3%) and performed as a catalyst to accelerate the decomposition of H₂O₂. A peroxide detection assay was then used to detect H₂O₂ after 2D-MnO₂ treatment and demonstrated increased ROS-scavenging, whereby a greater absorbance indicates a higher concentration of H₂O₂ (Figure 3d). Oxygen gas formation from H₂O₂ decomposition can be visualized after incubation with NHPH, which could potentially act as a source of oxygen and help alleviate hypoxic microenvironments during injury or degeneration (Figure 3e). Meanwhile, it is crucial to investigate if the bubble formation would harm the cell viability in the future, as acoustic cavitation of microbubbles on cell membranes during sonoporation is known to disrupt cell membranes or even inhibit tumor proliferation.⁴⁹

Additionally, NHPH composed of enzyme-like 2D-MnO₂ nanosheets can be fully degraded via redox reaction through naturally secreted reductants, such as ascorbic acid (vitamin C) or glutathione (Figure 3f).^{50–53} As a result, NHPHs are fully degradable through (i) a redox mechanism for the degradation of 2D-MnO₂ nanosheets and (ii) proteolytic degradation of synthetic peptides. Notably, the degradation rate can be tuned through the concentration of 2D-MnO₂ nanosheets within NHPH (Figure 3i). Besides, the rates at which drugs are released from biomaterials can be adjusted to optimize the release of therapeutics for improved treatment of acute or chronic inflammatory states. Degenerative conditions such as IVD may require a more sustained release of drugs and growth factors to combat chronic inflammation and cell death. However, burst-release kinetics of encapsulated biomolecules that often occur in current drug delivery systems are not desired for the treatment of

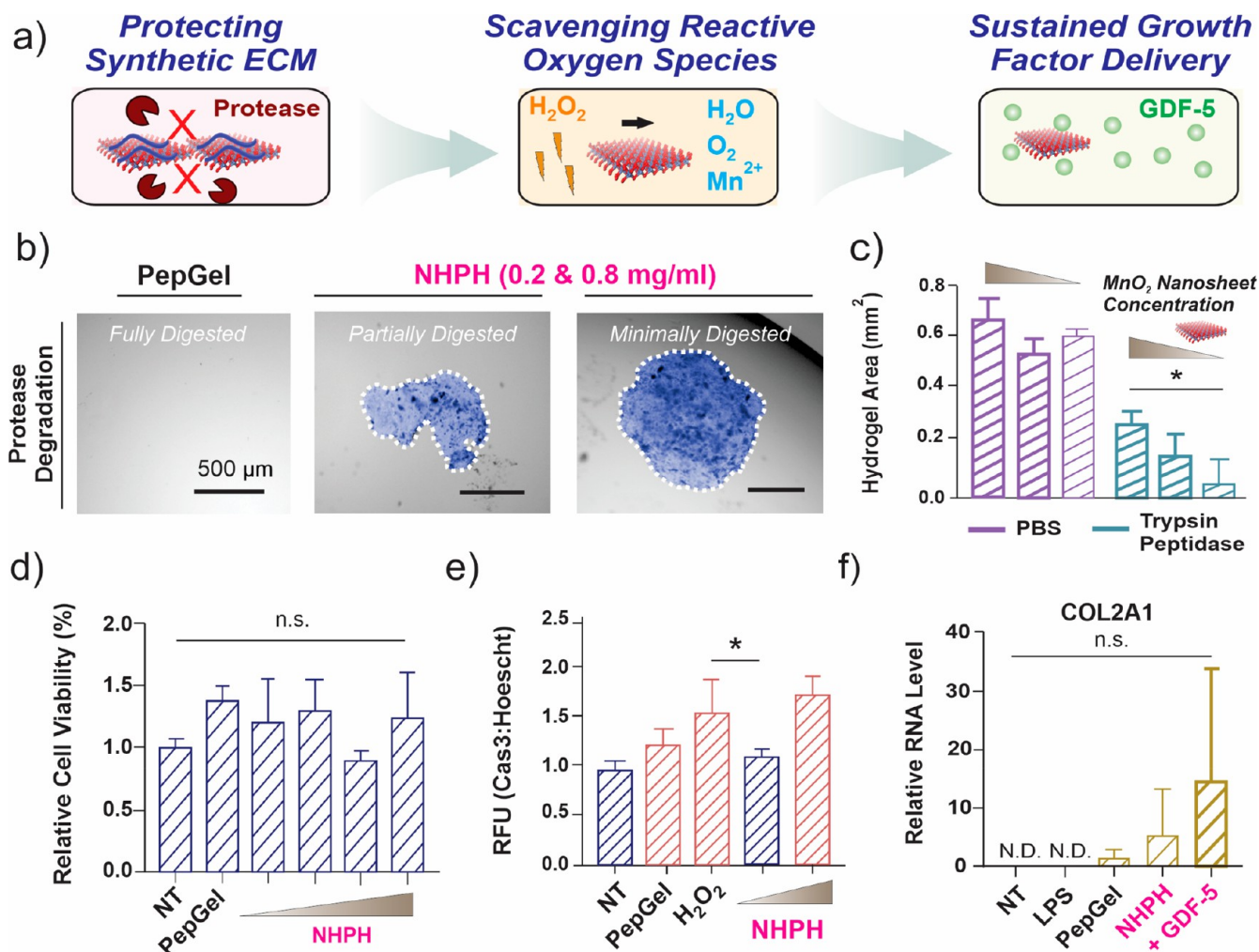


Figure 4. Nanomaterial-enhanced biophysical properties and growth factor delivery promote therapeutic outcomes *in vitro*. (a) Incorporating 2D-MnO₂ nanosheets to form NHPH can confer several therapeutic advantages such as delaying proteolytic degradation of essential peptide fibrils, scavenging ROS (i.e., H₂O₂) to suppress inflammation, and promoting ECM deposition (i.e., collagen II) through growth factor delivery. (b) Degradation of hydrogels in the presence of a serine protease, trypsin demonstrating that increasing MnO₂ concentration delays protease digestion of peptides in NHPH ($n = 3$, 0.8 mg/mL, 0.2 mg/mL MnO₂ concentration represent middle and right images, respectively). (c) Quantification of hydrogel area after proteolytic degradation via trypsin. Bolded groups represent those with 2D-MnO₂ nanosheets (0.2 and 0.8 mg/mL), while those not bolded represent PepGel group (hydrogel with no nanomaterials) ($n = 3$, $*p = 0.01$). (d) Cell viability of nucleus pulposus cells incubated with NHPH containing a range of 2D-MnO₂ nanosheet concentrations (0.1, 0.2, 0.3, 0.4 mg/mL from left to right). (e) Quantification of immunostaining for apoptotic marker, cleaved caspase 3 (Cas3) in human nucleus pulposus cells after being treated with NHPH-scavenged peroxide (H₂O₂) solution. MnO₂ concentrations are 0.2 and 0.8 mg/mL from left to right ($n = 3$, $*p = 0.03$). (f) Delivery of growth factors (GDF-5) to human IVD nucleus pulposus cells and resulting gene expression of collagen II subunit A1 (COL2A1), the most abundant type of collagen in the nucleus pulposus region ($n = 3$). The error bars are standard deviation around mean, $n = 3$ experimental replicates for all experiments. Statistical analysis by ordinary one-way ANOVA with Tukey's multiple comparisons test. n.s. means no significance.

chronic inflammation. To evaluate the high drug loading and release rate of growth factor from NHPH, a model growth factor, fluorescein isothiocyanate-conjugated insulin (FITC-insulin, 0.2 mg/mL), was loaded in NHPH. Compared to hydrogels with no 2D-MnO₂ nanosheets (i.e., PepGel), NHPH with 2D-MnO₂ nanosheets showed a more sustained release of FITC-insulin, providing the potential to treat injuries requiring sustainable, localized drug release as opposed to global intravenous administration of biomolecules which rapidly diffuse and have short-lived effects (Figure 3h).

Finally, delivering a detectable chemical signal to monitor *in vivo* drug release and biomaterial degradation is a difficulty that needs to be addressed. Fluorescence-based probes are limited because of the low penetrance of visible light. On the other hand,

MRI has been widely employed as a noninvasive *in vivo* imaging method and can monitor biomaterial degradation. NHPHs containing 2D-MnO₂ nanosheets degrade via a reduction in the water and (Mn²⁺) ion, a well-characterized MRI contrast agent. Fully degraded NHPH (via ascorbic acid treatment) loaded with FITC-insulin release Mn²⁺ ion contrast agent and FITC-insulin in a concentration-dependent manner, providing the advantage of correlating drug release with biomaterial degradation (Figure 3g and Figure S2).

To elucidate the potential therapeutic effects of NHPHs on *in vivo* disc repair, we first evaluate NHPH biological properties *in vitro* (Figure 4). First, as previously reported, a major limitation of synthetic peptide-derived ECM hydrogels is their susceptibility to rapid proteolytic degradation (Figure 4a). While fully

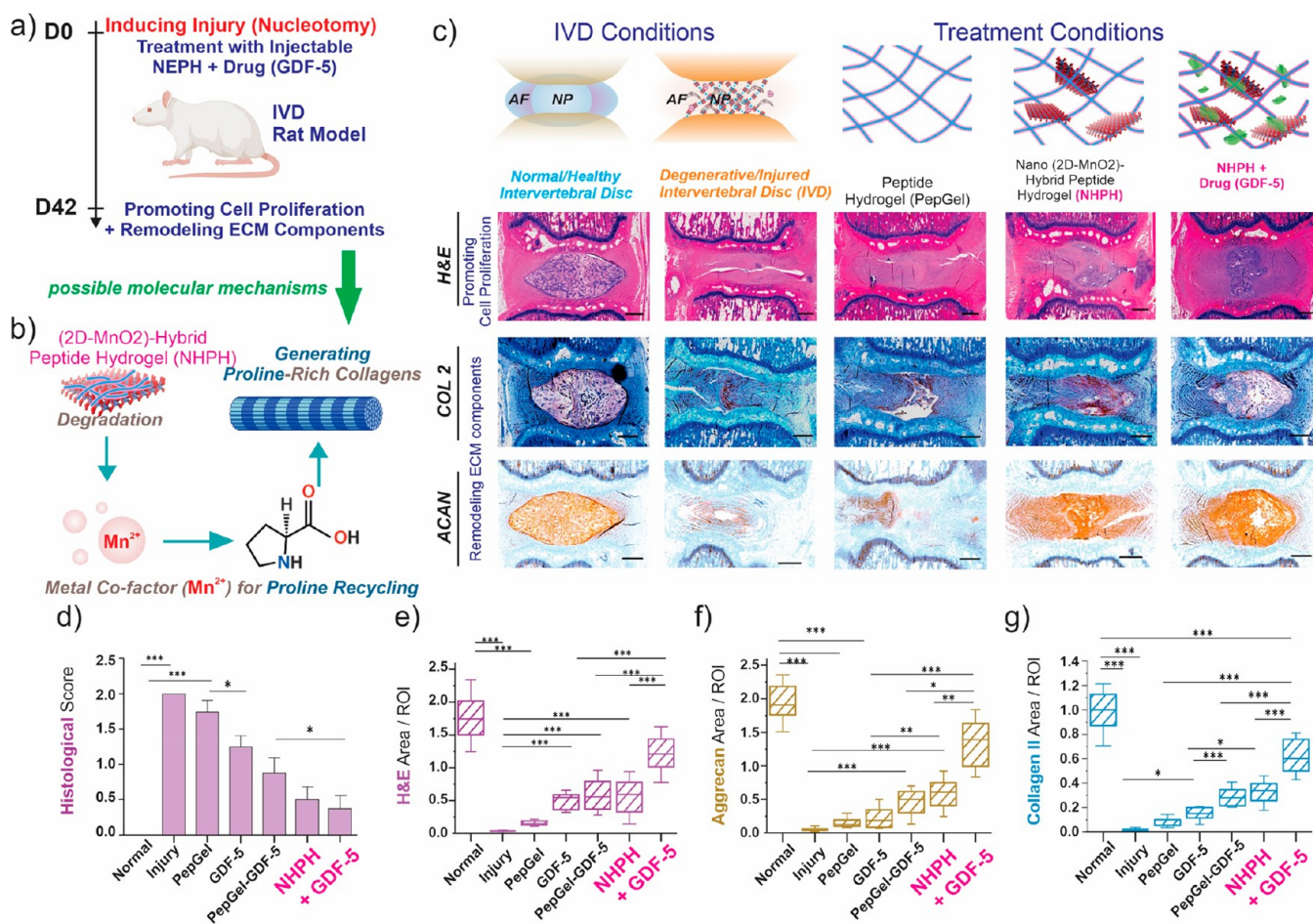


Figure 5. NHPH promotes cellular proliferation and regeneration of favorable ECM components such as collagen and aggrecan in a rat IVDD model. (a) A degenerated IVD model was induced by performing a nucleotomy in rats followed by immediate injection of hydrogels. (b) Degradation of MnO₂ nanosheets releases Mn²⁺ ion which is an essential metal cofactor in prolydase activity. Collagen II is rich in proline and enhanced prolydase activity may promote collagen recycling and provide a more favorable ECM microenvironment for tissue regeneration. (c) Experimental groups were injected postnucleotomy and 6 weeks later analyzed for regeneration including H&E staining, IHC for COL2, and ACAN showing NHPH loaded with GDF-5 hydrogel exhibited greatest cell proliferation, collagen synthesis, and aggrecan deposition, demonstrating the therapeutic potential of IOM hydrogels to provide anti-inflammation, growth factor delivery, and favorable degradation byproducts (i.e., Mn²⁺, O₂, and H₂O). (d–g) Histological score and quantification of H&E and IHC staining. Mean ± SEM, (*n* = 8), one-way ANOVA followed by Tukey's post-test. ****p* < 0.0001 scale bars, 500 μm.

biodegradable materials are advantageous, the rapid degradation of synthetic ECM may hinder tissue regeneration and overall injury repair over the long-term. To this end, we prepared NHPH and investigated the rate of proteolytic degradation in the presence of a serine protease which reportedly cleaves at lysine and arginine residues in octapeptides. NHPHs were incubated in concentrated trypsin solution (10 mg/mL) overnight, and hydrogel size was quantified by ImageJ (Figure 4b,c and Figure S3). Proteases are heavily secreted during severe degeneration and injury and are closely associated with pain induction. As a consequence, NHPHs with increasing 2D-MnO₂ nanosheet demonstrate the potential to delay proteolytic degradation during IVD degenerative microenvironment. This could be used further to tune the biomaterial degradation rate and retain the integrity of synthetic ECM *in vivo*. Next, we aimed to evaluate the ROS-scavenging effect of NHPH in a biological system *in vitro* using primary human nucleus pulposus cells (hNPCs) (Figure 4d). First, we confirmed the cell viability of NHPH with increasing concentrations of 2D-MnO₂ nanosheets (Figure 4g). Next, NHPHs (0.2 mg/mL, 0.8 mg/mL MnO₂ nanosheet concentration) were incubated in a solution of H₂O₂

(0.3%) and mixed for approximately 5 min to scavenge ROS and decompose H₂O₂ to water and oxygen gas. Next, the solution was added to hNPC cell culture media and cultured overnight. As a result, the cell viability (presto blue assay) revealed that cell survival was higher in NHPH with relatively lower concentrations (0.2 mg/mL) compared to those treated with solely 300 μM H₂O₂. (Figure S4). Interestingly, 500 μM treatment of H₂O₂ alone to hNPCs showed a wide range of cell viability (Figure S4). Furthermore, higher MnO₂ nanosheet concentrations (0.8 mg/mL) were observed to trigger an adverse cellular response; therefore, subsequent *in vivo* studies in NHPH used a MnO₂ nanosheet concentration of 0.1 mg/mL to avoid severe side effects.

Immunostaining for apoptosis marker cleaved caspase-3 (Cas3) demonstrated a similar trend to cell viability where the Cas3 to DAPI ratio, normalized to the nontreated control, was lowest in both nontreated and NHPH with a 0.2 mg/mL concentration of 2D-MnO₂ nanosheets embedded within (Figure 4e and Figures S5 and S6). These results imply that the scavenging of H₂O₂ species (i.e., ROS) from NHPH may protect hNPCs from elevated expression caspase and under-

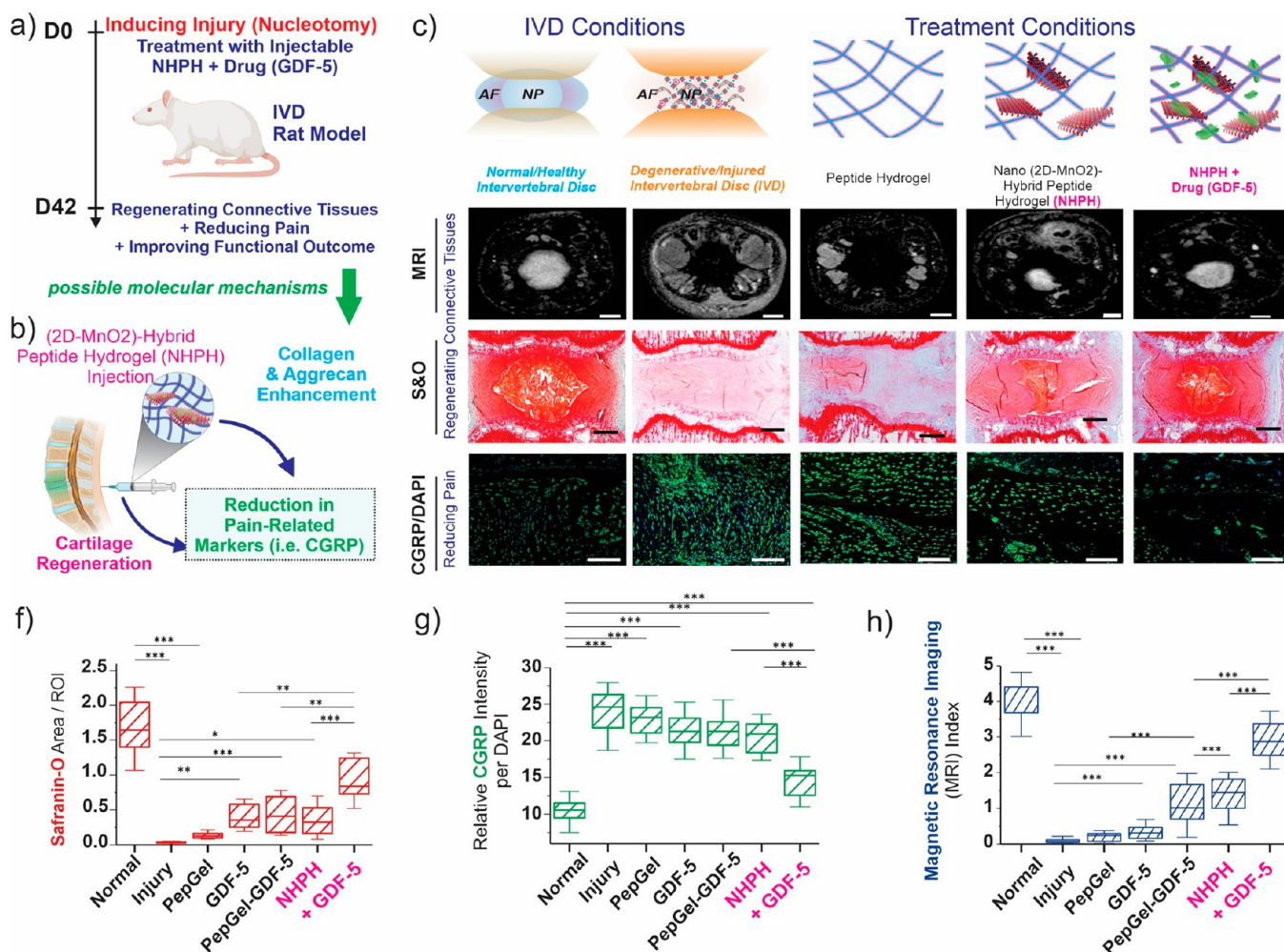


Figure 6. NHPH regenerates connective tissue and reduced pain markers in a rat IVDD model to potentially improve functional outcomes. (a) IVDD was induced in a rat model by performing a nucleotomy followed by immediate injection of hydrogel (b) to improve ECM formation and alleviate pain associated with degenerated disc including T2-weighted MRI of experimental groups after 6 weeks compared to normal, uninjured discs, exhibiting strong signal intensity from NHPH loaded with GDF-5; Safranin-O staining demonstrating robust cartilage regeneration after injection of NHPH loaded with GDF-5; and immunostaining for CGRP, a pain-related marker, showing the lowest intensity for NHPH with GDF-5. (f–h) Quantification of S&O staining, CGRP intensity, and T2-MRI signal intensity, all reaching similar quantification levels to normal IVDs. Mean \pm SEM, ($n = 8$), one-way ANOVA followed by Tukey's post-test. *** $p < 0.0001$ scale bars, 500 μm .

going apoptosis. Last, it has been reported that growth factors can stimulate IVD cells to produce ECM proteins and promote cellular proliferation.^{54–56} To this end, we investigated growth factor delivery of GDF-5-loaded NHPH using a Transwell cell culture model. Here, GDF-5-loaded NHPHs were inserted into the top chamber while hNPCs were cultured in the bottom chamber. After stimulating hNPCs to an inflammatory state by administering lipopolysaccharide (LPS, 10 $\mu\text{g}/\text{mL}$), hydrogels were added to the top chamber and cultured overnight. Gene expression of collagen II (COL2A1) was then investigated with quantitative polymerase chain reaction and showed that GDF-5 loaded NHPH had the highest COL2A1 expression, followed by NHPH without GDF-5 and PepGel alone (Figure 4i). Pro-inflammatory cytokine levels (CXCL1, IL-6, IL-1B, and MMP-13) were also investigated (Figure S7). This result may be due to the fact that (i) GDF-5 has been reported to stimulate collagen 2 expression and (ii) the octapeptide sequence in NHPH (FEFKFEFK) had been reported to stimulate IVD cell proliferation.⁴³ Furthermore, the Mn^{2+} ion has been linked to enhanced collagen expression by acting as an essential metal

cofactor in the enzyme prolydase, which is responsible for producing the amino acid proline.⁵⁷

Next, the *in vitro* therapeutic properties of NHPHs prompted us to investigate their potential in disc repair *in vivo*. As a proof-of-concept, we tested GDF-5-loaded NHPH in a rat nucleotomy model, as its inflammatory profiles and heterogeneous ECM degeneration properties have been well studied and are suitable for testing injectable biomaterials in disc regeneration. We hypothesized that NHPH drug-loaded with GDF-5 would aid tissue regeneration by establishing an ECM-mimicking micro-environment, scavenging ROS after nucleotomy, and stimulating cellular proliferation and ECM synthesis. To this end, a nucleotomy (complete removal of the nucleus pulposus region of the IVD) was performed on Sprague–Dawley rats, and 10 mL of NHPHs loaded with GDF-5 (10 $\mu\text{g}/\text{mL}$) were immediately injected into the injury site along with NHPH without GDF-5, PepGel alone, GDF-5 saline solution, and PepGel-GDF-5 (Figure 5a,b and Figure S8). Rats were sacrificed at week 6 (day 42) and analyzed to investigate tissue regeneration within the NP, AF, and end plate regions. Hematoxylin and eosin (H&E) staining of the injury site at 6 weeks showed NHPH with

2D-MnO₂ nanosheets loaded with GDF-5 regenerated distinct AF and NP regions dense with cellular nuclei and ECM components, yielding the lowest histological score of all experimental groups (Figure 5c). Compared to all the other experimental groups, the distance between adjacent end plates in rats injected with NHPH or NHPH with GDF-5 appears to be much greater (Figure 5c). Moreover, it has been well established that the NP region contains chondrocyte-like cells that readily express and secrete ECM proteins such as collagen II (COL2) and essential proteoglycans such as aggrecan (ACAN) to support the gelatinous and flexible structure of the IVD.⁵⁸ Thus, immunohistochemistry (IHC) in the NP region indicated the highest expression for COL2 in the NHPH loaded with GDF-5 condition, thus restoring a favorable ECM microenvironment (Figure 5c).

This outcome might be attributed to several factors, including the ROS-scavenging effect of 2D-MnO₂ nanosheets, the sustained delivery of GDF-5 from 2D-MnO₂ nanosheets, and the nanosheet-fibril composite's ECM-mimicking structure. In addition, manganese ions (Mn²⁺) have also been reported as essential metal ions for prolydase activity, an enzyme involved in the hydrolysis of proline and hydroxyproline, which makes up a significant portion of collagen protein.⁵⁷ The degradation of NHPH and release of Mn²⁺ ions may have accelerated the recycling of collagen protein and efficient ECM remodeling compared to groups without 2D-MnO₂ nanosheets by providing a localized source of Mn²⁺ ions. Furthermore, there have been reports suggesting the high water content and gel-like features of the NP area are controlled by aggrecan expression from NP cells.⁵⁹ Here, aggrecan levels were highly elevated in NHPH loaded with GDF-5 compared to all other experimental groups (Figure 5d–g). We hypothesize this result may be due to the sustained release of growth factor from GDF-5 loaded 2D-MnO₂ nanosheets, which has been reported to stimulate NP cell proliferation, ECM gene synthesis, and ACAN expression. Peptide and saline groups showed minimal aggrecan expression after 6 weeks. Moreover, GDF-5 alone showed decreased aggrecan expression, which could be attributed to the short-term therapeutic effects of a burst release of growth factors.

Interestingly, NHPH without GDF-5 loaded on 2D-MnO₂ nanosheets also demonstrated increased aggrecan expression compared to peptide and GDF-5 alone groups. Though the detailed mechanisms require further investigation, this may be due to the therapeutic effects of Mn²⁺ ions, a byproduct of NHPH degradation. It has been previously reported that Mn²⁺ ions can provide a protective effect of hyaluronan, which closely interacts with aggrecan to form supramolecular structures of ECM.⁶⁰ Next, we investigated more clinically relevant outcomes such as IVD regeneration and pain alleviation (Figure 6a,b and Figures S8, S10, and S11). Moreover, noninvasive T2-weighted MRI analysis confirmed that NHPH with GDF-5 restored high water content to the degenerated IVD region (Figure 6c and Figure S9). Given that peptide hydrogels displayed limited T2-weighted MRI signal, this result is most likely related to tissue regeneration rather than hydrogel water retention. Indeed, following the regeneration of collagen and aggrecan because of NHPH with GDF-5, we also showed enhanced ECM formation in degenerated IVD (Figure 6a,b).

With the outcome of *in vitro* and *in vivo* assays, we sought to evaluate NHPH for pain reduction, which has been challenging using current tissue engineering approaches. Previously, it has been reported that even moderate cases of IVDD cause chronic back pain, decreasing quality of life.^{61–63} Therefore, we

investigated the expression of Calcitonin gene-related peptide (CGRP), a known biomarker of perceived pain in nociceptive pathways in the nervous system. Excitingly, 6-weeks post-injection, CGRP levels in NHPH with GDF-5 were drastically reduced compared to injured discs and all other conditions, suggesting a reduction in pain sensation (Figure 6d,g). An analysis of the inflammation 6-weeks postinjection of NHPH with GDF-5 showed an increase in both M1 (pro-inflammatory) and M2 (anti-inflammatory) macrophage phenotypes, where elevated levels of Iba1, CD86, and CD163 were observed (Figures S11 and S12). Additionally, the reduction of pain markers is also consistent with enhancement in motor movement evaluation. Specifically, the Von Frey test that uses the withdrawal reflex of mice in response to punctation stimulus was performed from week 2 (day 14) to week 6 (day 42). Based on the 50% withdrawal threshold value, NHPH with GDF-5-treated mice exhibited a significant enhancement compared to both controls of NHPH only and no treatment (Figure S13). Moreover, at week 5 and week 6, withdrawal threshold values of NHPH with GDF-5 were statistically significant ($p < 0.05$) compared to peptide hydrogels alone (Figure S13). Therefore, NHPH successfully loaded with therapeutic growth factors reduced pain-related biomarker CGRP, which likely translated into a reduction in the Von Frey evaluation and improved functional outcomes.

CONCLUSIONS

In summary, we generated nanohybrid peptide hydrogels (NHPHs) to provide a versatile hybrid nanomaterial designed to stimulate regeneration in the intervertebral disc (IVD) injured area. NHPH with hierarchal structures demonstrated biomimetic mechanical properties that mimic natural collagen ECM at the nanoscale as well as microscale, while providing 3D-printing macroscale capabilities over conventional polymeric hydrogel materials used for biomedical applications such as gelatin or alginate. Although hierarchical structures have been previously applied for modulation of regenerative cell behaviors, our NHPH is injectable, thus representing clear advantages over traditional approaches.^{64–68} We further show that NHPHs have superior biophysical features due to nanomaterial-mediated accelerated drug release, tunable biodegradation, ROS scavenging, and MRI activity. However, due to the multifunctionality of NHPH, it is unclear which therapeutic function of NHPH is making the most significant contributions to the fibrocartilaginous tissue regeneration, necessitating future studies on its mechanism. Furthermore, the addition of growth differentiation factor 5 (GDF-5) in NHPH promoted an ECM-stimulating effect *in vitro* and *in vivo*. NHPHs loaded with GDF-5 were injected into a nucleotomy rat model to regenerate lost tissue in the AF and NP regions. After 6 weeks, we demonstrated enhanced ECM regeneration (i.e., collagen and aggrecan), cellular proliferation, and T2-MRI signal intensity compared to both PepGel hydrogels and growth factors alone. Histological analysis at 6 weeks shows IVD regeneration with NHPH, while behavioral analysis demonstrated a positive trend. Overall, NHPHs significantly improved IVD repair following nucleotomy and partially restored a healthy ECM microenvironment to allow NF and AF regeneration. Future studies may explore utilizing nanomaterial-based hydrogels for NP or progenitor cell encapsulation and transplantation into the IVD injury sites. More precisely tailoring the NHPH stiffness to fit the differentiation toward nucleolus pulposus cells as well as revealing the mechanism behind NHPH-enhanced nucleolus

pulposus regeneration would be essential for designing better scaffolds in the future. The combination of cellular components and a biomaterial to provide a favorable ECM microenvironment could yield even better tissue regeneration and pain alleviation. The understanding of dynamic mechanical, biochemical, and biological properties of NHPH under *in vivo* and disease-like microenvironments would also facilitate the design of better biomaterials for treating fibrocartilaginous injuries and other diseases and disorders.

METHODS

Synthesis of MnO₂ Nanosheets. To synthesize MnO₂ nanosheets, a reported redox reaction-based strategy was adapted. Briefly, 10 mL 0.6 M tetramethylammonium pentahydrate aqueous solution was mixed with 10 mL 6 wt % H₂O₂ aqueous solution. Next, the mixed solution was quickly injected into a 0.3 M MnCl₂ solution under vigorous stirring. An hour later, the stirring speed was reduced to 300 rpm, and the reaction was continued overnight. The dark-colored product was collected by 3000 rpm centrifugation and washed with ethanol and water for 3 times each. The final product was oven-dried at under 60° in the air. After redissolving and tip-sonicating the dried samples in water, a stable MnO₂ nanosheet suspension can be obtained. The suspension can be stored at room temperature for one month without any noticeable aggregation or degradation.

Synthesis of Nanohybrid Peptide Hydrogel. NHPHs were synthesized by first weighing out lyophilized peptides (FEFKFEFK, Biomatik). Next, phosphate buffer solution (for experiments of *in vitro* cell culture, ROS, and *in vivo* experiments) or nuclease-free water was dissolved to desired concentration (10–20 mg/mL) in microcentrifuge tubes through vigorous mixing. Samples were then vortexed for 30 s and centrifuged for 30 s (1000 rpm) to fully dissolve the peptides and remove bubble formation. Steps were repeated as necessary to ensure components were fully dissolved. For NHPH, MnO₂ nanosheets (3 mg/mL) were added to PepGel hydrogels and vigorously mixed with PepGels, vortexed, and centrifuged as aforementioned. Additional rounds of vortexing and centrifugation may be required to distribute nanosheets homogeneously. A light brown color should be homogeneous throughout the hydrogel solution.

Atomic Force Microscopy Experiment. NHPH were synthesized according to the previously described protocol. Next, 10 μ L of diluted NHPH (5 mg/mL, 100 μ g/mL) were drop-cast on mica substrates (Ted Pella) and placed in a desiccator at 23 °C (room temperature) for 2 h until dried. Mica substrates were then clamped to the stage of a Park Systems AFM. The noncontact mode was used to measure substrate topography in the deposited region.

Transmission Electron Microscopy Experiment. NHPH were synthesized according to the previously described protocol. After diluting to desired concentrations, approximately 5 μ L of hydrogel sample was drop-cast onto transmission electron microscopy (TEM) grids and placed at 23 °C (room temperature) for 2 h in a desiccator until fully dried. Samples were then imaged using a Philips CM12 electron microscope. TEM images of NHPH fibers were pseudocolored using Photoshop and fiber length/width were quantified using ImageJ analysis.

Scanning Electron Microscopy Experiment. NHPH were synthesized according to the previously described protocol; however, nuclease-free water was used to dissolve lyophilized peptide as opposed to phosphate buffer saline (PBS) to prevent salt formation postlyophilization and to prevent sample charging under the electron beam. Samples were then para-film and placed at –80 °C overnight. Samples were then removed from –80 °C and lyophilized for 48 h under vacuum. Next, samples were carefully removed from the plastic tubes and placed on SEM grids (TED Pella) covered with carbon tape, taking care so as not to deform the lyophilized hydrogels with excessive force. Lyophilized NHPH were then placed in an ion sputter coater (Electron Microscopy Sciences 150T ES) and pumped down. Then, gold (20 nm) was sputter-coated on each sample. Afterward, samples

were loaded into a Zeiss Sigma Scanning electron microscope and imaged using an SE2 detector at 5 kV.

Confocal Microscopy. NHPH were synthesized according to the previously described protocol to yield a final concentration of 10 μ M of thioflavin T (dissolved in water), a final peptide concentration of 20 mg/mL, and a final concentration of 0.2 mg/mL of 2D-MnO₂ nanosheets. Beforehand, 2D-MnO₂ nanosheets were coated with rhodamine B (RhB) overnight. For this, 2D-MnO₂ nanosheets (3 mg/mL) were incubated in RhB (1 mM) overnight with light shaking. Afterward, PBS was added dropwise, and the solution was spun down at 8000 rpm for 5 min to precipitate 2D-MnO₂ nanosheets. The coated nanosheets were washed and centrifuged with water three times and resuspended in water. Just before imaging, 20 μ L of NHPH hydrogel was drop-cast on a single clean glass slide (75 mm \times 25 mm). Afterward, another clean glass slide (25 mm \times 25 mm) was gently placed on top to prevent the microscope objective from contacting the hydrogel material and permit confocal imaging. Lastly, Z-stack images were taken with a Zeiss LSM 800 confocal microscope.

Thioflavin T Assay. PepGel hydrogels were synthesized according to the previously described protocol. Ten μ M of ThT in water was added to dissolve lyophilized peptide (FEFKFEFK) to yield PepGel hydrogels with a final peptide concentration of 20 mg/mL. Next, 20 μ L of peptide hydrogels were drop-cast into 96-well plates. PBS was added (180 μ L) to fully submerged the hydrogel. Then, fluorescence intensity (440 nm excitation and 482 nm emission) was measured using a Tecan Microplate Reader and normalized to PBS as a control. Control groups were directly pipetted (200 μ L) into 96-well plates.

Rheometry Experiment. NHPH were synthesized according to the previously described protocol. Next, 200 μ L of hydrogel was dispensed onto the platform of a Kinexus Ultra Rotational Rheometer (Malvern Instruments). First, an amplitude sweep was performed. Then, a single strain oscillatory test was performed under a frequency of 1 Hz, 1% strain, at a 0.25 mm gap. *G'* or elastic components are plotted using the values at 30-s increments.

Synthesis of GDF5-Functionalized Nanosheets and Hybridization with Peptide Hydrogel. To prepare GDF5-functionalized MnO₂ nanosheets, we first dissolved GDF5 (Peprotech, catalog no. 120-01) in ultrapure water at a concentration of 1.0 mg/mL. Next, GDF-5 (1.0 mg/mL) solution was dropwise added into MnO₂ (3 mg/mL) nanosheet aqueous solution at approximately a 1:3 ratio (v/v) under shaking. The mixed solution was continued with shaking overnight at room temperature, then transferred into the peptide hydrogel precursor solution in PBS to yield a final concentration of 0.1 mg/mL MnO₂ nanosheets and 10 μ g/mL GDF-5. Next, samples were mixed and pipetted several times, and a light-brown hybrid hydrogel was then formed. Samples were then vortexed for 30 s and centrifuged briefly to ensure a homogeneous distribution of 2D-MnO₂ nanosheets. Control hydrogels without MnO₂ nanosheets or GDF5 peptides were also fabricated using similar procedures.

At the beginning of the surgery, the peritoneal site was sterilized with 70% alcohol. Afterward, rats were thoroughly anesthetized with a general anesthesia mixture of Zoletil (50 mg/kg Virbac Laboratories, France) and Rompun (10 mg/kg, Bayer, Korea) injected intraperitoneally. Then, the proximal-most part of the tail and the pelvic area were sterilized with 70% alcohol, followed by a povidone-iodine solution. A longitudinal incision of 1 cm was made along the tail to expose the lateral portion of the coccygeal disc. Subsequently, a #11 scalpel blade was inserted 1.5 mm into the coccygeal disc (Co4–5, Co5–6); then, nucleotomy was performed by disc AF incision and NP aspiration with a 22-gauge catheter on a 5-ml syringe. Nucleotomy at Co4–5 was performed to assess the effects of materials in 29 rats. Thereafter, intradiscally 10 μ L injection of peptide hydrogel, GDF-5 saline solution, peptide hydrogel+GDF-5, MnO₂+peptide hydrogel and MnO₂+peptide hydrogel+GDF-5 was injected by using a 25-gauge catheter. Finally, the skin was sutured, disinfected, and an appropriate dose of analgesic (Ketoprofen, SCD Pharm. Co. Ltd., Korea) and antibiotic (Cefazolin, CKD Pharmaceuticals, Korea) for 3 days after surgery was provided. The whole surgical procedure was performed on heating pads to maintain the body temperature of rats.

Animal Model Nucleotomy. In total, eight-week-old female Sprague–Dawley rats (220–240 g) were purchased from Orient Bio Inc., Korea, and were acclimatized for a week at a life/dark cycle of 12/12 h (temperature; 22 ± 1 °C and relative humidity; $50\% \pm 1\%$) and free approach to food and water. The animal experiments were performed according to the direction approved by the Institutional Animal Care and Use Committee (IACUC) of CHA Bundang Medical Center (IACUC 200141).

Animal Experimental Design. Twenty-nine rats were randomly divided into five groups for the experiment. Group 1: peptide hydrogel, group 2: GDF-5- saline solution, group 3: peptide hydrogel+GDF-5, group 4: MnO_2 +peptide hydrogel, and group 5: MnO_2 +peptide hydrogel+GDF-5. Each group contains 6 animals except group 1, which contains only 5 animals. After 6 weeks of implantation, coccygeal discs were harvested for radiologic and histologic analysis.

Cell Viability. NHPH hydrogels (20 mg/mL peptide concentration) of varying 2D- MnO_2 nanosheet concentrations (0.1, 0.2, 0.3, 0.4 mg/mL) were synthesized according to the described protocol, and 5 μL of hydrogel was pipetted into wells of a 96 well plate. Next, wells were coated with poly L-lysine (PLL, 2 $\mu\text{g}/\text{cm}^2$ in water) according to ScienCell manufacturer's protocol dictating overnight. Then, the wells were washed carefully with PBS to remove excess PLL, which could cause cytotoxicity. Afterward, Nucleus pulposus cells purchased from Science Cell (cat no. 4800) were thawed at 37 °C and seeded at 10,000 cells/ cm^2 in 200 μL of nucleus pulposus cell media (ScienCell hNPC medium, cat no. 4801) with 10% FBS, 1% Pen/strep, and 1% nucleus pulposus cell growth supplement (ScienCell, cat nos. 0010, 0503, and 4852, respectively). After 24 h postseeding, nucleus pulposus cell media was changed to remove residual DMSO, washed with PBS, and every replaced with fresh media. Media changes were performed every 2–3 days as recommended by the manufacturer. After 5 days, PrestoBlue (ThermoFisher) reagent (20 μL) was added to each well of media (200 μL) and incubated at 37 °C for 15 min. Afterward, fluorescence intensity (excitation: 560 nm; emission: 590 nm) was measured (iTecan Microplate Reader) and normalized to control (no treatment).

ROS-Induced Apoptosis. NHPH hydrogels (20 mg/mL) of varying 2D- MnO_2 nanosheet concentrations (0.2, 0.8 mg/mL) were synthesized according to the described protocol. To initiate cell culture, wells were coated with poly L-lysine (2 $\mu\text{g}/\text{cm}^2$) overnight. The next day, wells were washed several times with PBS to remove excess PLL. Nucleus pulposus cells purchased from Science Cell (cat no. 4800) were thawed at 37 °C and seeded at 10,000 cells/ cm^2 . Nucleus pulposus cell media (ScienCell hNPC medium, cat no. 4801) with 10% FBS, 1% Pen/strep, and 1% nucleus pulposus cell growth supplement (ScienCell, cat nos. 0010, 0503, and 4852, respectively) was changed 24 h postseeding to remove residual DMSO and every 2 days thereafter. After reaching approximately 70% confluency, a solution of H_2O_2 (H_2O_2 , 0.3%) (Fischer Scientific, cat. no. H325-500) was separately prepared. Then, 20 μL of NHPH hydrogels were mixed with 300 μL of diluted H_2O_2 solutions for approximately 2 min. For control groups, H_2O_2 was added to cell culture wells to yield both 300 μM and 500 μM concentrations for positive control groups. For experimental groups, 20 μL of hydrogel (NHPH or PepGel) was mixed with 300 μL of H_2O_2 (0.3%) solutions for approximately 2 min. Then, equal parts volume as the 500 μM positive control group of the hydrogel+ H_2O_2 mixture was added to the cell culture well. After 24 h, a PrestoBlue (ThermoFisher) assay was performed (20 μL PrestoBlue reagent for every 200 μL) as previously described, and fluorescence intensities (excitation: 560 nm; emission: 590 nm) were recorded and normalized to control (no treatment) using a Tecan Microplate Reader.

3D Printing of NHPH. 3D Printing was tested using an EnvisionTEC 3D Bioplotter Manufacturer Series printer (EnvisionTEC, Inc., Dearborn, MI). A 3D model of 10 mm W \times 10 mm L \times 1.5 mm H was designed in Sketchup (Google, Inc., Mountain View, CA) and exported as STL files to Perfactory Rapid Prototype (RP) (EnvisionTEC, Inc., Dearborn, MI) to translate the STL file into a g-code. The g-code was then exported to the 3D Bioplotter. NHPH were prepared at 10 mg/mL concentration in diH_2O and loaded into disposable plastic syringe. The model was printed at RT and 0.1 bar

pressure at a speed of 2.5 mm/s with a 1 mm continuous strand distance, a z-offset of 0.32 mm, and no contour. The inner diameter of the nozzle was 400 μm (22 gauge).

Cleaved Caspase 3/Hoechst/Actin Staining. NHPH hydrogels (20 mg/mL) of varying 2D- MnO_2 nanosheet concentrations (0.2, 0.8 mg/mL) were synthesized according to the described protocol. To initiate cell culture, wells were coated with PLL (2 $\mu\text{g}/\text{cm}^2$) overnight. The next day, wells were washed several times with PBS to remove excess PLL. Nucleus pulposus cells purchased from Science Cell (cat no. 4800) were thawed at 37 °C and seeded at 10,000 cells/ cm^2 . Nucleus pulposus cell media (ScienCell hNPC medium, cat no. 4801) with 10% FBS, 1% Pen/strep, and 1% nucleus pulposus cell growth supplement (ScienCell, cat no. 0010, 0503, and 4852, respectively) was changed 24 h postseeding to remove residual DMSO and every 2 days thereafter. Hydrogel scavenging experiments were performed as previously described in ROS-induced apoptosis methods. Briefly, after reaching approximately 70% confluency, a solution of H_2O_2 (H_2O_2 , 0.3%) (Fischer Scientific, cat. no. H325-500) was separately prepared. Then, 20 μL of NHPH hydrogels were mixed with 300 μL of diluted H_2O_2 solutions (0.3%) for approximately 2 min. Control groups included a concentration of 300 μM H_2O_2 and equal parts volume as the control group was used for adding the hydrogel+ H_2O_2 mixture to the cell culture media. After 24 h, cells were fixed with incubation in formalin solution neutral buffered, 10% (Sigma-Aldrich, cat no. HT501128), washed several times with PBS, and stored at 4 °C. For immunostaining, PBS was aspirated, and fixed cells were incubated at 4 °C overnight in a blocking buffer (X% NGS, X% Triton X-100). Then, cleaved caspase-3 primary antibody (Asp175) (source: rabbit) (Abcam, cat no. 9661) was diluted 1:500 in antibody dilution buffer, treated to each well, and stored overnight at 4 °C. Next, cells were washed several times with PBS and treated with secondary antirabbit Alexa Fluor 488 (ThermoFisher, cat. no. A-11008) (1:500 dilution). After 60 min, cells were washed several times with PBS. For Hoechst staining, Hoechst 33342 (ThermoFisher, cat. no. H1399) was diluted 1:1000 in PBS. Each well was then treated with the Hoechst solution for 30 min and then washed several times with PBS. Finally, the fluorescence intensity (excitation: 496 nm, emission: 519 nm) was measured with a Tecan Microplate Reader. Cas3/Hoechst was quantified and normalized to control. For actin staining, cells were treated with Alexa-Fluor 633 Phalloidin (ThermoFisher, cat. no. A2284). For the immunostaining images, exposure times for Hoechst, Cas3, and Actin were 100 ms, 3 s, and 300 ms, respectively. Immunostaining image LUTs in terms of min, γ , and max are set at 0, 1, and 200 (DAPI), 110, 1, and 730 (Cas3), and 0, 1, and 150 (Actin).

Hydrogel Degradation via Ascorbic Acid. NHPH hydrogels (20 mg/mL) of varying 2D- MnO_2 nanosheet concentrations (0.1, 0.2, and 0.4 mg/mL) were synthesized according to the described protocol, and 5 μL of hydrogel was pipetted into wells in a 96-well plate. Then, ascorbic acid (Sigma-Aldrich, cat. no. A92902) 0.1 mg/mL was added to each well, and absorbance at 600 nm was measured using a Tecan Microplate Reader in a time-dependent manner. Absorbance measurements were taken for 2.5 h. To calculate cumulative degradation percentage, maximum absorbance values were assigned as 0% degradation, while minimum absorbance values which plateaued were assigned as 100% degradation of MnO_2 nanosheets.

ROS-Scavenging. 2D- MnO_2 nanosheets, synthesized using previous protocols, were added to H_2O_2 solution from a 3 mg/mL stock solution at different concentrations (0.1, 0.2, 0.4 mg/mL) and at a ratio of 1:3 2D- MnO_2 nanosheets: H_2O_2 and mixed thoroughly. Simultaneously, a working reagent was prepared from Pierce Quantitative Peroxide Assay Kit (Aqueous) (ThermoFisher cat. no. 23280) according to the manufacturer's protocol. Twenty μL of sample and 200 μL of working reagent were mixed, and the assay was permitted to reach an end point for 15 min. Then, absorbance at 595 nm was measured using a Tecan Microplate Reader. Absorbance values were normalized to control (water).

MRI of NHPH Degradation and FITC-Insulin Release. First, FITC-Insulin (0.25 mg/mL) was purified using 3 kDa filter membranes (Amicon). Next, overnight, FITC-Insulin (0.25 mg/mL) was incubated with 2D- MnO_2 nanosheets (1:3 v/v%) under light shaking. Then, F.I.-

loaded NHPH hydrogels (0.1, 0.2, 0.4 mg/mL) were synthesized according to the previously described protocol. Next, 20 μ L NHPH hydrogels were treated with 600 μ L of ascorbic acid (Sigma-Aldrich, cat. no. A92902) at a concentration of 1 mg/mL to induce full nanosheet degradation in Mn^{2+} ion and water. Afterward, the solution was mixed for 30 s. Then, 200 μ L from each experimental group was placed in a 96-well plate, and the fluorescence intensity was measured (448 nm excitation and 525 nm emission) using a Tecan Microplate Reader from the released FITC-Insulin. Next, 180 μ L of solution from each experimental group was deposited into a removable well strip for MRI analysis. Additionally, a standard curve of manganese dichloride ($MnCl_2$) was included as a positive control. MRI was performed using an Aspect T1MRI. Quantification was done via ImageJ analysis, measuring the mean intensity of sample areas. Data points for MRI analysis were normalized to water, while data points for fluorescence release were normalized to the PepGel experimental group.

NHPH Drug Release. FITC-insulin (0.25 mg/mL) was purified using 3 kDa filter membranes (Amicon) and loaded/mixed into NHPH hydrogels with varying 2D- MnO_2 nanosheet concentration (0.2 mg/mL, 0.4 mg/mL, and 0.8 mg/mL). Hydrogels were centrifuged briefly and lightly vortexed to remove bubble formation and ensure homogeneous distribution of FITC-insulin. Simultaneously, a 1% bovine serum albumin (BSA) solution was prepared and used to coat the well surface of a 48-well plate to prevent nonspecific binding of released FITC-insulin. BSA solution was incubated at 37 °C overnight and washed several times with PBS to remove excess protein. Then, 20 μ L of hydrogel from each experimental group was pipetted into wells of a 48-well plate to which 1 mL of PBS was added. The well plate was then para-film to prevent evaporation of the solution and placed on a shaker with light shaking in a 37 °C incubator. At each time point, 100 μ L of supernatant was removed from the well and transferred to a 96-well plate for plate reader analysis and fluorescence intensity measurement using 448 nm excitation and 525 nm emission.

GDF-5 Delivery to HNPCS. NHPH hydrogels were synthesized according to previous protocols. GDF-5 (Peprotech) reconstituted in water was loaded on 2D- MnO_2 nanosheets (1:3 v/v%) overnight under light shaking at 4 °C. GDF-5 loaded 2D MnO_2 nanosheets were then used to from NHPH (0.2 mg/mL, 20 mg/mL, respectively). Meanwhile, a 24-well plate was coated with PLL at 2 μ g/cm². Nucleus pulposus cells purchased from Science Cell (cat no. 4800) were thawed at 37 °C and seeded at 10,000 cells/cm². Nucleus pulposus cell media (ScienCell hNPC medium, cat no. 4801) with 10% FBS, 1% Pen/strep, and 1% nucleus pulposus cell growth supplement (ScienCell, cat nos. 0010, 0503, and 4852, respectively) was changed 24 h postseeding to remove residual DMSO and every 3 days thereafter. Then, transwell cell culture inserts (Corning, cat. no. CLS3396) for 24-well culture plates were inserted into the well, and 20 μ L of NHPH hydrogel loaded with GDF-5 was pipetted into the upper chamber, followed by 100 μ L of hNPC media. Cells were cultured for 24 h and trizoled for downstream PCR analysis.

qRT-PCR for RNA Expression Level. Cell lysate was collected with trizol (Life Technologies) treatment for 2–3 min and placed at –80 °C. Next, RNA was precipitated and extracted for RT-PCR and qPCR. mRNA was converted into cDNA using the SuperScript III First-Strand Synthesis System (Life Technologies). qPCR was performed with Power SYBR Green Master Mix using a StepOne Plus PCR instrument (Applied Biosciences). Data points are plotted as RQ vs sample (relative RNA level) for biological replicates and RQ min/max for single replicates. Col2A1 primer sequences are as follows: *Forward 5'-3'*: TGGACGCCATGAAGGTTTTCT *Reverse 5'-3'*: TGGGAGCCAGATTGTCATCTC. CXCL1 primer sequences is as follows: *Forward 5'-3'*: TCACAGTGTGTGGTCAACAT *Reverse 5'-3'*: AGCCCCTTTGTTCTAAGCCA. IL-6 primer sequences is as follows: *Forward 5'-3'*: AAACAACCTGAACCTTCCAAAGA *Reverse 5'-3'*: GCAAGTCTCCTCATTGAATCCA. IL-1B primer sequences is as follows: *Forward 5'-3'*: ATGATGGCTTATTACAGTGGCAA *Reverse 5'-3'*: GTCGGAGATTTCGTAGCTGGA. MMP-13 primer sequences are as follows: *Forward 5'-3'*:

Proteolytic Hydrogel Degradation. NHPH hydrogels were synthesized according to previous protocols. Next, bovine trypsin

(Sigma-Aldrich) was dissolved in PBS at 10 mg/mL. Then, NHPH hydrogels and PepGel hydrogels were pipetted into 48-well plates, submerged in trypsin solution, and incubated in a 37 °C incubator overnight. After 24 h, the well plates were imaged using phase objectives on a Nikon Ti Series microscope. Hydrogel size was then quantified using ImageJ software.

Mechanical Allodynia. The Von Frey test was performed to assess mechanical allodynia induced by pain in the rats. It was performed 2 days before the surgery and on days 2, 7, 14, 21, 28, 35, and 42 days after the surgery. First, to avoid the exploratory activities of rats, they were placed individually into a six-compartment rat enclosure with wire mesh floors and lids with air holes for 20 min habituation period. After that, on the ventral surface of the tail, a 2-g filament was applied for a maximum of 6 s with enough force. Positive responses were judged to be behaviors that occurred immediately or within 6 s, such as flinching, licking, withdrawing, or shaking the base of the tail. However, if the animals did not show any responses to the filaments when it was applied, then it was considered as a negative response. The test was carried out five times for each animal from each group. The two independent observers who were blinded by the specimen's treatment were involved in Von Frey's analysis.

MRI. After 6 weeks of implantation, 9.4T MRI (Bruker BioSpec, USA) was performed to study the changes in the structure of the disc and degree of degeneration of the coccygeal disc, signal intensity, and presence of water content in the disc. T2-weighted imaging for the coronal plane was performed as time to repetition (TR) of 5000 ms, time to echo (TE) of 30 ms, 150 horizontal_150 vertical matrix; field of view of 15 horizontal \times 15 verticals, and 0.5 mm slices with 0 mm spacing between each slice. The signal intensity and MRI index (calculated as the area of NP multiplied by average signal intensity) were calculated in order to evaluate the degree of degeneration of the coccygeal disc. The high signal intensity area in the midcoronal plane of the T2 weighted images was considered as a region of interest (ROI), as the outline of the NP. The ROI was measured by using ImageJ software (the National Institutes of Health, Bethesda, MD, USA) (1). The two independent observers who were blinded by the specimen's treatment were involved in measuring the MRI index.

Safranin-O Staining with Histological Scoring and H&E Staining. Histological analysis was performed after the 6 weeks of implantation. Rats were euthanized, and discs from each rat were harvested for histological analysis. The discs with the adjacent vertebral body were fixed in 10% neutral buffered formalin for 1 week, and decalcified in Rapid Cal Immuno (BBC Biochemical, Mount Vernon, WA, USA) for 2 weeks. Afterward, tissues were processed for paraffin embedding and sectioning into coronal sections (10 μ m) using a microtome (Leica). The obtained sections were dewaxed, rehydrated, and stained with Safranin-O (Sigma, USA) to analyze the quantity and distribution of proteoglycan content. Finally, sections were mounted using mounting media and scanned with an OLYMPUS C-mount camera adapter (U-TVO.63XC, Tokyo, Japan). Similarly, histological scoring was performed utilizing an extensive 8-point scale for measuring IVD based on safranin-O staining. The scoring was based on the NP cellularity (0–2), AF morphology (0–2), NP matrix (0–2) and the boundary between NP and AF (0–2), resulting in four subcategories. In this case, nondegenerative characteristics were zero, mild degenerative characteristics were represented as one, and severe degenerative change was represented as two (2). The pathologists, who were completely blinded to the sample information, analyzed all the samples for histological analysis. Furthermore, the obtained sections were dewaxed, rehydrated, and stained with H&E to evaluate the tissue morphology and proteoglycan distribution.

Immunohistochemistry. After 6 weeks of implantation, rats were euthanized via excess carbon dioxide inhalation and coccygeal discs were collected, and immunohistochemical analysis was performed for aggrecan (disc matrix component), collagen type II (a component of disc NP matrix), CGRP (pain-marker), Iba1 (pan-macrophage), CD86 (M1-macrophage) and CD163(M2-macrophage). The harvested tissues were fixed overnight in a 4% paraformaldehyde (PFA) solution and decalcified using a decalcification solution; RapidCal Immuno (BBC Biochemical, Mount Vernon, WA, USA), for 2 weeks. Then, discs

were embedded within paraffin wax and sectioned longitudinally using a microtome (Leica) into sections of 5–10 μm thickness. For the immunohistochemical staining, the first sections were dewaxed, rehydrated, and after that, stained with primary antibodies against aggrecan (1:1000, Abcam, UK), collagen type II (1:100, Abcam, UK) CGRP (1:200, Abcam, UK), Iba-1 (1:200, Abcam, UK), CD86 (1:200, Abcam, UK) and CD163 (1:200, Abcam, UK). Then, after 24 h of incubation, sections were washed with phosphate-buffered saline with Tween 20 and again incubated with the secondary antibody anti-Rb horseradish peroxidase (Roche Diagnostics Ltd., Switzerland), and Alexa Fluor 488, 568, and 647-conjugated secondary antibodies (1:400, Invitrogen, USA). After that, specimens were carried out for the washing step; then, the specimens were counter-stained with DAPI (1:500, Abcam, UK) and incubated for 10 min. The sections were mounted and finally examined using a fluorescence microscope (Zeiss 880, Germany and Leica SP5, Germany). The percentage of the positive area and cell number relative to DAPI was calculated by using ImageJ Software (<https://imagej.nih.gov/ij/>).

In Vivo Statistical Analysis. For the statistical analysis of data, GraphPad Prism (version 5.01, GraphPad Software) was used, and ImageJ software (<https://imagej.nih.gov/ij/>) was used for the quantification of data. Data are presented as mean \pm standard error of the mean (SEM). One-way analysis of variance (ANOVA) with the Tukey posthoc test was used to assess the effects of multiple treatments in *in vivo* experiments, and *p*-values <0.05 were considered statistically significant.

ASSOCIATED CONTENT

Supporting Information

The Supporting Information is available free of charge at <https://pubs.acs.org/doi/10.1021/acsnano.2c11441>.

Figures illustrating magnetic resonance imaging and quantification of NEP hydrogels, characterization of proteolytic degradation of NEP hydrogels, cell viability assay of hNPCs and NHPH hydrogels, immunostaining of apoptotic markers within nucleus pulposus cells, immunostaining of apoptotic markers within nucleus pulposus cells, relative RNA levels of chemokines and cytokines of nucleus pulposus cells, representative images of aggrecan and collagen II staining, T2-weighted MRI of the coccygeal discs 6 weeks after treatment, alleviation of injury-induced pain phenotype, immunohistochemistry of macrophage phenotype after treatment, quantification of macrophage phenotype after treatment, characterization of a pain model induced by IVD injury (PDF)

AUTHOR INFORMATION

Corresponding Authors

Inbo Han – Department of Neurosurgery, CHA University School of Medicine, Seongnam-si, Gyeonggi-do 13497, Korea; Email: hanib@cha.ac.kr

Ki-Bum Lee – Department of Chemistry and Chemical Biology, Rutgers, The State University of New Jersey, Piscataway, New Jersey 08854, United States; orcid.org/0000-0002-8164-0047; Email: kblee@rutgers.edu

Authors

Brian M. Conley – Department of Chemistry and Chemical Biology, Rutgers, The State University of New Jersey, Piscataway, New Jersey 08854, United States

Letao Yang – Department of Chemistry and Chemical Biology, Rutgers, The State University of New Jersey, Piscataway, New Jersey 08854, United States; orcid.org/0000-0002-0572-9787

Basanta Bhujel – Department of Neurosurgery, CHA University School of Medicine, Seongnam-si, Gyeonggi-do 13497, Korea
Jeffrey Luo – Department of Chemistry and Chemical Biology, Rutgers, The State University of New Jersey, Piscataway, New Jersey 08854, United States; orcid.org/0000-0002-0140-1370

Complete contact information is available at:
<https://pubs.acs.org/doi/10.1021/acsnano.2c11441>

Author Contributions

[§]These authors contributed equally.

Notes

The authors declare no competing financial interest.

ACKNOWLEDGMENTS

The authors would like to acknowledge the assistance of Dr. Jinho Yoon for atomic force microscopy imaging, Derek Adler for magnetic resonance imaging assistance, and Dr. Cemile Bektaş for 3D-printing assistance. We are also grateful for Hyunjun Jang and Yannan Hou's assistance in synthesizing nanosheets. Ki-Bum Lee acknowledges the partial financial support from the NSF (CBET-1803517), the New Jersey Commission on Spinal Cord (CSCR17IRG010; CSCR16ERG019), NIH R21 (R21AR071101), and NIH R01 (1R01DC016612, 3R01DC016612-01S1, and 5R01DC016612-02S1), Alzheimer's Association (AARG-NTF-21-847862), N.J. Commission on Cancer Research (COCR23PPR007), and HealthAdvanced (NHLBI, U01HL150852). Jeffrey Luo acknowledges the fellowship from the NIH Postdoctoral Training for Translating Research in Regenerative Medicine (NIH T32EB005583). Dr. Inbo Han acknowledges funding support from the following agency: Korea Health Technology Research and Development Project, Ministry for Health, and Welfare Affairs HR16C0002.

REFERENCES

- (1) Soos, B.; Szentpetery, A.; Raterman, H. G.; Lems, W. F.; Bhattoa, H. P.; Szekanecz, Z. Effects of targeted therapies on bone in rheumatic and musculoskeletal diseases. *Nature Reviews Rheumatology* **2022**, *18* (5), 249–257.
- (2) Bonnevie, E. D.; Gullbrand, S. E.; Ashinsky, B. G.; Tsinman, T. K.; Elliott, D. M.; Chao, P. H. G.; Smith, H. E.; Mauck, R. L. Aberrant mechanosensing in injured intervertebral discs as a result of boundary-constraint disruption and residual-strain loss. *Nature Biomedical Engineering* **2019**, *3* (12), 998–1008.
- (3) Zehra, U.; Tryfonidou, M.; Iatridis, J. C.; Illien-Junger, S.; Mwale, F.; Samartzis, D. Mechanisms and clinical implications of intervertebral disc calcification. *Nature Reviews Rheumatology* **2022**, *18* (6), 352–362.
- (4) Gullbrand, S. E.; Ashinsky, B. G.; Bonnevie, E. D.; Kim, D. H.; Engles, J. B.; Smith, L. J.; Elliott, D. M.; Schaer, T. P.; Smith, H. E.; Mauck, R. L. *Science Translational Medicine* **2018**, *10* (468), eaau0670.
- (5) Han, W. M.; Heo, S. J.; Driscoll, T. P.; Delucca, J. F.; McLeod, C. M.; Smith, L. J.; Duncan, R. L.; Mauck, R. L.; Elliott, D. M. Microstructural heterogeneity directs micromechanics and mechanobiology in native and engineered fibrocartilage. *Nat. Mater.* **2016**, *15* (4), 477–484.
- (6) Wyse Jackson, T.; Michel, J.; Lwin, P.; Fortier, L. A.; Das, M.; Bonassar, L. J.; Cohen, I. Structural origins of cartilage shear mechanics. *Science Advances* **2022**, *8* (6), eabk2805.
- (7) Kurowska-Stolarska, M.; Alivernini, S. Synovial tissue macrophages in joint homeostasis, rheumatoid arthritis and disease remission. *Nature Reviews Rheumatology* **2022**, *18* (7), 384–397.
- (8) Risbud, M. V.; Shapiro, I. M. Role of cytokines in intervertebral disc degeneration: pain and disc content. *Nature Reviews Rheumatology* **2014**, *10* (1), 44–56.

- (9) Zhu, J. J.; Yang, S. H.; Qi, Y. D.; Gong, Z.; Zhang, H. T.; Liang, K. Y.; Shen, P. Y.; Huang, Y. Y.; Zhang, Z.; Ye, W. L.; Yue, L.; Fan, S. W.; Shen, S. Y.; Mikos, A. G.; Wang, X. M.; Fang, X. Q. Stem cell-homing hydrogel-based miR-29b-5p delivery promotes cartilage regeneration by suppressing senescence in an osteoarthritis rat model. *Science Advances* **2022**, *8* (13), eabk0011.
- (10) Ran, J. S.; Fei, Y.; Wang, C. L.; Ruan, D. F.; Hu, Y. J.; Zheng, Z. F.; Chen, X.; Yin, Z.; Tang, C. Q.; Chen, Y. W.; Huang, J. Y.; Shen, L. F.; Wu, L. D.; Heng, B. C.; Pioletti, D.; Shen, W. L.; Ouyang, H. W. An Off-the-Shelf Tissue Engineered Cartilage Composed of Optimally Sized Pellets of Cartilage Progenitor/Stem Cells. *ACS Biomaterials Science & Engineering* **2021**, *7* (3), 881–892.
- (11) Wang, S. Q.; Yang, L. T.; Cai, B. L.; Liu, F. W.; Hou, Y. N.; Zheng, H.; Cheng, F.; Zhang, H. P.; Wang, L.; Wang, X. Y.; Lv, Q. X.; Kong, L.; Lee, K. B.; Zhang, Q. Y. Injectable hybrid inorganic nanoscaffold as rapid stem cell assembly template for cartilage repair. *National Science Review* **2022**, *9* (4), nwa037.
- (12) Murphy, M. P.; Koepke, L. S.; Lopez, M. T.; Tong, X. M.; Ambrosi, T. H.; Gulati, G. S.; Marecic, O.; Wang, Y. T.; Ransom, R. C.; Hoover, M. Y.; Steininger, H.; Zhao, L. M.; Walkiewicz, M. P.; Quarto, N.; Levi, B.; Wan, D. C.; Weissman, I. L.; Goodman, S. B.; Yang, F.; Longaker, M. T.; Chan, C. K. F. Articular cartilage regeneration by activated skeletal stem cells. *Nature Medicine* **2020**, *26* (10), 1583–1592.
- (13) Loebel, C.; Burdick, J. A. Engineering Stem and Stromal Cell Therapies for Musculoskeletal Tissue Repair. *Cell Stem Cell* **2018**, *22* (3), 325–339.
- (14) Sakai, D.; Andersson, G. B. Stem cell therapy for intervertebral disc regeneration: obstacles and solutions. *Nature Reviews Rheumatology* **2015**, *11* (4), 243–256.
- (15) Kwon, H.; Brown, W. E.; Lee, C. A.; Wang, D. A.; Paschos, N.; Hu, J. C.; Athanasiou, K. A. Surgical and tissue engineering strategies for articular cartilage and meniscus repair. *Nature Reviews Rheumatology* **2019**, *15* (9), 550–570.
- (16) Lyu, F. J.; Cheung, K. M.; Zheng, Z. M.; Wang, H.; Sakai, D.; Leung, V. Y. IVD progenitor cells: a new horizon for understanding disc homeostasis and repair. *Nature Reviews Rheumatology* **2019**, *15* (2), 102–112.
- (17) Sloan, S. R.; Wipplinger, C.; Kirnaz, S.; Navarro-Ramirez, R.; Schmidt, F.; McCloskey, D.; Pannellini, T.; Schiavinato, A.; Hartl, R.; Bonassar, L. J. Combined nucleus pulposus augmentation and annulus fibrosus repair prevents acute intervertebral disc degeneration after discectomy. *Sci. Transl. Med.* **2020**, *12* (534), 2380.
- (18) Li, C.; Chen, J.; Lv, Y.; Liu, Y.; Guo, Q.; Wang, J.; Wang, C.; Hu, P.; Liu, Y. Recent Progress in Electrospun Nanofiber-Based Degenerated Intervertebral Disc Repair. *ACS Biomaterials Science & Engineering* **2022**, *8* (1), 16–31.
- (19) Marshall, S. L.; Jacobsen, T. D.; Emsbo, E.; Murali, A.; Anton, K.; Liu, J. Z.; Lu, H. H.; Chahine, N. O. Three-Dimensional-Printed Flexible Scaffolds Have Tunable Biomimetic Mechanical Properties for Intervertebral Disc Tissue Engineering. *ACS Biomaterials Science & Engineering* **2021**, *7* (12), 5836–5849.
- (20) Sun, B.; Lian, M.; Han, Y.; Mo, X.; Jiang, W.; Qiao, Z.; Dai, K. A 3D-Bioprinted dual growth factor-releasing intervertebral disc scaffold induces nucleus pulposus and annulus fibrosus reconstruction. *Bioactive materials* **2021**, *6* (1), 179–190.
- (21) Sun, Z.; Luo, B.; Liu, Z.; Huang, L.; Liu, B.; Ma, T.; Gao, B.; Liu, Z.-H.; Chen, Y.-F.; Huang, J.-H.; et al. Effect of perfluorotributylamine-enriched alginate on nucleus pulposus cell: Implications for intervertebral disc regeneration. *Biomaterials* **2016**, *82*, 34–47.
- (22) Takeoka, Y.; Yurube, T.; Morimoto, K.; Kunii, S.; Kanda, Y.; Tsujimoto, R.; Kawakami, Y.; Fukase, N.; Takemori, T.; Omae, K.; et al. Reduced nucleotomy-induced intervertebral disc disruption through spontaneous spheroid formation by the Low Adhesive Scaffold Collagen (LASCOL). *Biomaterials* **2020**, *235*, 119781.
- (23) Tong, W.; Lu, Z.; Qin, L.; Mauck, R. L.; Smith, H. E.; Smith, L. J.; Malhotra, N. R.; Heyworth, M. F.; Caldera, F.; Enomoto-Iwamoto, M.; et al. Cell therapy for the degenerating intervertebral disc. *Translational Research* **2017**, *181*, 49–58.
- (24) Uysal, O.; Arslan, E.; Gulseren, G.; Kilinc, M. C.; Dogan, I.; Ozalp, H.; Caglar, Y. S.; Guler, M. O.; Tekinay, A. B. Collagen peptide presenting Nanofibrous scaffold for intervertebral disc regeneration. *ACS Applied Bio Materials* **2019**, *2* (4), 1686–1695.
- (25) Vaudreuil, N.; Henrikson, K.; Pohl, P.; Lee, A.; Lin, H.; Olsen, A.; Dong, Q.; Dombrowski, M.; Kang, J.; Vo, N.; et al. Photopolymerizable biogel scaffold seeded with mesenchymal stem cells: safety and efficacy evaluation of novel treatment for intervertebral disc degeneration. *Journal of Orthopaedic Research* **2019**, *37* (6), 1451–1459.
- (26) Guo, J. L.; Kim, Y. S.; Xie, V. Y.; Smith, B. T.; Watson, E.; Lam, J.; Pearce, H. A.; Engel, P. S.; Mikos, A. G. Modular, tissue-specific, and biodegradable hydrogel cross-linkers for tissue engineering. *Science Advances* **2019**, *5* (6), eaaw7396.
- (27) Isa, I. L. M.; Abbah, S. A.; Kilcoyne, M.; Sakai, D.; Dockery, P.; Finn, D. P.; Pandit, A. Implantation of hyaluronic acid hydrogel prevents the pain phenotype in a rat model of intervertebral disc injury. *Science Advances* **2018**, *4* (4), eaaq0597.
- (28) Lin, W. F.; Kluzek, M.; Iuster, N.; Shimoni, E.; Kampf, N.; Goldberg, R.; Klein, J. Cartilage-inspired, lipid-based boundary-lubricated hydrogels. *Science* **2020**, *370* (6514), 335–338.
- (29) Nerurkar, N. L.; Baker, B. M.; Sen, S.; Wible, E. E.; Elliott, D. M.; Mauck, R. L. Nanofibrous biologic laminates replicate the form and function of the annulus fibrosus. *Nat. Mater.* **2009**, *8* (12), 986–992.
- (30) Yang, R. H.; Li, G.; Zhuang, C. Y.; Yu, P.; Ye, T. J.; Zhang, Y.; Shang, P. Y.; Huang, J. J.; Cai, M.; Wang, L.; Cui, W. G.; Deng, L. F. Gradient bimetallic ion-based hydrogels for tissue microstructure reconstruction of tendon-to-bone insertion. *Science Advances* **2021**, *7* (26), eabg3816.
- (31) Freedman, B. R.; Mooney, D. J. Biomaterials to Mimic and Heal Connective Tissues. *Adv. Mater.* **2019**, *31* (19), 1806695.
- (32) Isa, I. L. M.; Mokhtar, S. A.; Abbah, S. A.; Fauzi, M. B.; Devitt, A.; Pandit, A. Intervertebral Disc Degeneration: Biomaterials and Tissue Engineering Strategies Towards Precision Medicine. *Adv. Healthcare Mater.* **2022**, *11*, 2102530.
- (33) Chameettachal, S.; Midha, S.; Ghosh, S. Regulation of chondrogenesis and hypertrophy in silk fibroin-gelatin-based 3D bioprinted constructs. *ACS Biomaterials Science & Engineering* **2016**, *2* (9), 1450–1463.
- (34) Dikina, A. D.; Almeida, H. V.; Cao, M.; Kelly, D. J.; Alsberg, E. Scaffolds derived from ECM produced by chondrogenically induced human MSC condensates support human MSC chondrogenesis. *ACS Biomaterials Science & Engineering* **2017**, *3* (7), 1426–1436.
- (35) de Melo, B. A.; Jodat, Y. A.; Mehrotra, S.; Calabrese, M. A.; Kamperman, T.; Mandal, B. B.; Santana, M. H.; Alsberg, E.; Leijten, J.; Shin, S. R. 3D printed cartilage-like tissue constructs with spatially controlled mechanical properties. *Adv. Funct. Mater.* **2019**, *29* (51), 1906330.
- (36) Hodgkinson, T.; Kelly, D. C.; Curtin, C. M.; O'Brien, F. J. Mechanosignaling in cartilage: an emerging target for the treatment of osteoarthritis. *Nature Reviews Rheumatology* **2022**, *18* (2), 67–84.
- (37) Walker, C. J.; Crocini, C.; Ramirez, D.; Killaars, A. R.; Grim, J. C.; Aguado, B. A.; Clark, K.; Allen, M. A.; Dowell, R. D.; Leinwand, L. A.; Anseth, K. S. Nuclear mechanosensing drives chromatin remodeling in persistently activated fibroblasts. *Nature Biomedical Engineering* **2021**, *5* (12), 1485–1499.
- (38) Peng, B.; Hao, J.; Hou, S.; Wu, W.; Jiang, D.; Fu, X.; Yang, Y. Possible pathogenesis of painful intervertebral disc degeneration. *Spine* **2006**, *31* (5), 560–566.
- (39) Alvarez, Z.; Kolberg-Edelbrock, A. N.; Sasselli, I. R.; Ortega, J. A.; Qiu, R.; Syrgiannis, Z.; Mirau, P. A.; Chen, F.; Chin, S. M.; Weigand, S.; Kiskinis, E.; Stupp, S. I. Bioactive scaffolds with enhanced supra-molecular motion promote recovery from spinal cord injury. *Science* **2021**, *374* (6569), 848–856.
- (40) Edelbrock, A. N.; Alvarez, Z.; Simkin, D.; Fyrner, T.; Chin, S. M.; Sato, K.; Kiskinis, E.; Stupp, S. I. Supramolecular Nanostructure Activates TrkB Receptor Signaling of Neuronal Cells by Mimicking Brain-Derived Neurotrophic Factor. *Nano Lett.* **2018**, *18* (10), 6237–6247.

- (41) Shoulders, M. D.; Raines, R. T. Collagen structure and stability. *Annual review of biochemistry* **2009**, *78*, 929–958.
- (42) Loebel, C.; Saleh, A. M.; Jacobson, K. R.; Daniels, R.; Mauck, R. L.; Calve, S.; Burdick, J. A. Metabolic labeling of secreted matrix to investigate cell-material interactions in tissue engineering and mechanobiology. *Nat. Protoc.* **2022**, *17* (3), 618–648.
- (43) Ligorio, C.; Zhou, M.; Wychowanec, J. K.; Zhu, X.; Bartlam, C.; Miller, A. F.; Vijayaraghavan, A.; Hoyland, J. A.; Saiani, A. Graphene oxide containing self-assembling peptide hybrid hydrogels as a potential 3D injectable cell delivery platform for intervertebral disc repair applications. *Acta biomaterialia* **2019**, *92*, 92–103.
- (44) Holmes, D. F.; Lu, Y.; Starborg, T.; Kadler, K. E. Collagen fibril assembly and function. *Current topics in developmental biology* **2018**, *130*, 107–142.
- (45) Li, J. Y.; Mooney, D. J. Designing hydrogels for controlled drug delivery. *Nature Reviews Materials* **2016**, *1* (12), 1–17.
- (46) Iatridis, J. C.; Weidenbaum, M.; Setton, L. A.; Mow, V. C. Is the nucleus pulposus a solid or a fluid? Mechanical behaviors of the nucleus pulposus of the human intervertebral disc. *Spine* **1996**, *21* (10), 1174–1184.
- (47) Suzuki, S.; Fujita, N.; Hosogane, N.; Watanabe, K.; Ishii, K.; Toyama, Y.; Takubo, K.; Horiuchi, K.; Miyamoto, T.; Nakamura, M.; et al. Excessive reactive oxygen species are therapeutic targets for intervertebral disc degeneration. *Arthritis Res. Ther.* **2015**, *17* (1), 1–17.
- (48) Huang, Y.-C.; Urban, J. P.; Luk, K. D. Intervertebral disc regeneration: do nutrients lead the way? *Nature Reviews Rheumatology* **2014**, *10* (9), 561–566.
- (49) Son, S.; Kim, J.; Kim, J.; Kim, B.; Lee, J.; Kim, Y.; Li, M.; Kang, H.; Kim, J. S. Cancer therapeutics based on diverse energy sources. *Chem. Soc. Rev.* **2022**, *51*, 8201–8215.
- (50) Deng, R.; Xie, X.; Vendrell, M.; Chang, Y.-T.; Liu, X. Intracellular glutathione detection using MnO₂-nanosheet-modified upconversion nanoparticles. *J. Am. Chem. Soc.* **2011**, *133* (50), 20168–20171.
- (51) Khan, Z.; Kumar, P.; Kabir-ud-Din. Kinetics of the reduction of water-soluble colloidal MnO₂ by ascorbic acid. *J. Colloid Interface Sci.* **2005**, *290* (1), 184–189.
- (52) Li, N.; Diao, W.; Han, Y.; Pan, W.; Zhang, T.; Tang, B. MnO₂-modified persistent luminescence nanoparticles for detection and imaging of glutathione in living cells and in vivo. *Chemistry—A European Journal* **2014**, *20* (50), 16488–16491.
- (53) Li, W.; Liu, Z.; Liu, C.; Guan, Y.; Ren, J.; Qu, X. Manganese dioxide nanozymes as responsive cytoprotective shells for individual living cell encapsulation. *Angew. Chem., Int. Ed.* **2017**, *56* (44), 13661–13665.
- (54) Feng, C.; Liu, H.; Yang, Y.; Huang, B.; Zhou, Y. Growth and differentiation factor-5 contributes to the structural and functional maintenance of the intervertebral disc. *Cellular Physiology and Biochemistry* **2015**, *35* (1), 1–16.
- (55) Masuda, K. Biological repair of the degenerated intervertebral disc by the injection of growth factors. *European Spine Journal* **2008**, *17* (4), 441–451.
- (56) Luo, X.-w.; Liu, K.; Chen, Z.; Zhao, M.; Han, X.-w.; Bai, Y.-g.; Feng, G. Adenovirus-mediated GDF-5 promotes the extracellular matrix expression in degenerative nucleus pulposus cells. *Journal of Zhejiang University-SCIENCE B* **2016**, *17* (1), 30–42.
- (57) Eni-Aganga, I.; Lanaghan, Z. M.; Balasubramaniam, M.; Dash, C.; Pandhare, J. PROLIDASE: A Review from Discovery to its Role in Health and Disease. *Frontiers in Molecular Biosciences* **2021**, *8*, 849723003.
- (58) Kluba, T.; Niemeyer, T.; Gaissmaier, C.; Gründer, T. Human annulus fibrosus and nucleus pulposus cells of the intervertebral disc: effect of degeneration and culture system on cell phenotype. *Spine* **2005**, *30* (24), 2743–2748.
- (59) Kepler, C. K.; Ponnappan, R. K.; Tannoury, C. A.; Risbud, M. V.; Anderson, D. G. The molecular basis of intervertebral disc degeneration. *Spine Journal* **2013**, *13* (3), 318–330.
- (60) Valachová, K.; Kogan, G.; Gemeiner, P.; Soltés, L. Protective effects of manganese (II) chloride on hyaluronan degradation by oxidative system ascorbate plus cupric chloride. *Interdisciplinary toxicology* **2010**, *3* (1), 26.
- (61) Altun, I. Cytokine profile in degenerated painful intervertebral disc: variability with respect to duration of symptoms and type of disease. *Spine Journal* **2016**, *16* (7), 857–861.
- (62) Hiyama, A.; Suyama, K.; Sakai, D.; Tanaka, M.; Watanabe, M. Correlational analysis of chemokine and inflammatory cytokine expression in the intervertebral disc and blood in patients with lumbar disc disease. *Journal of Orthopaedic Research* **2022**, *40* (5), 1213–1222.
- (63) Molinos, M.; Almeida, C. R.; Caldeira, J.; Cunha, C.; Gonçalves, R. M.; Barbosa, M. A. Inflammation in intervertebral disc degeneration and regeneration. *J. R. Soc., Interface* **2015**, *12* (104), 20141191.
- (64) Armstrong, J. P. K.; Pchelintseva, E.; Treumuth, S.; Campanella, C.; Meinert, C.; Klein, T. J.; Hutmacher, D. W.; Drinkwater, B. W.; Stevens, M. M. Tissue Engineering Cartilage with Deep Zone Cytoarchitecture by High-Resolution Acoustic Cell Patterning. *Adv. Healthcare Mater.* **2022**, *11* (24), 2200481.
- (65) Barcellona, M. N.; Speer, J. E.; Fearing, B. V.; Jing, L.; Pathak, A.; Gupta, M. C.; Buchowski, J. M.; Kelly, M.; Setton, L. A. Control of adhesive ligand density for modulation of nucleus pulposus cell phenotype. *Biomaterials* **2020**, *250*, 120057.
- (66) Bridgen, D. T.; Fearing, B. V.; Jing, L.; Sanchez-Adams, J.; Cohan, M. C.; Guilak, F.; Chen, J.; Setton, L. A. Regulation of human nucleus pulposus cells by peptide-coupled substrates. *Acta biomaterialia* **2017**, *55*, 100–108.
- (67) Maynard, S. A.; Gelmi, A.; Skaalure, S. C.; Pence, I. J.; Lee-Reeves, C.; Sero, J. E.; Whittaker, T. E.; Stevens, M. M. Nanoscale Molecular Quantification of Stem Cell–Hydrogel Interactions. *ACS Nano* **2020**, *14* (12), 17321–17332.
- (68) Navarro, Y.; Bleich-Kimelman, N.; Hazanov, L.; Mironi-Harpaz, I.; Shachaf, Y.; Garty, S.; Smith, Y.; Pelled, G.; Gazit, D.; Seliktar, D.; et al. Matrix stiffness determines the fate of nucleus pulposus-derived stem cells. *Biomaterials* **2015**, *49*, 68–76.